Vehicle induced turbulence and atmospheric pollution

Paul A. Makar[1], Craig Stroud[1], Ayodeji Akingunola[1], Junhua Zhang[1], Shuzhan Ren[1], Philip Cheung[1], Qiong Zheng[1]

[1]Air Quality Modelling and Integration Section, Air Quality Research Division, Atmospheric Science and Technology Directorate, Environment and Climate Change Canada, 4905 Dufferin Street, Toronto, Ontario, M3H 5T4, Canada

Correspondence to: Paul A. Makar (paul.makar@canada.ca)

Abstract. Theoretical models of the Earth's atmosphere adhere to an underlying concept of flow driven by radiative transfer and the nature of the surface over which the flow is taking place: heat from the sun and/or anthropogenic sources are the sole sources of energy driving atmospheric constituent transport. However, another source of energy is prevalent in the human environment at the very local scale – the transfer of kinetic energy from moving vehicles to the atmosphere. We show that this source of energy, due to being co-located with combustion emissions, can influence their vertical distribution to the extent of having a significant influence on lower troposphere pollutant concentrations throughout North America. The effect of vehicle-induced turbulence on freshly emitted chemicals remains notable even when taking into account more complex urban radiative transfer-driven turbulence theories at high resolution. We have designed a parameterization to account for the at-source vertical transport of freshly emitted pollutants from mobile emissions resulting from vehicle-induced turbulence, in analogy to sub-grid-scale parameterizations for plume rise emissions from large stacks. This parameterization allows vehicle-induced turbulence to be represented at the scales inherent in 3D chemical transport models, allowing this process to be represented over larger regions than is currently feasible with large eddy simulation models. Including this sub-grid-scale parameterization for the vertical transport of emitted pollutants due to vehicle-induced turbulence into a 3D chemical transport model of the atmosphere reduces pre-existing North American nitrogen dioxide biases by a factor of eight, and improves most model performance scores for nitrogen dioxide, particulate matter and ozone (for example, reductions in root mean square errors of 20, 9 and 0.5 percent, respectively).

1 Introduction

A common and ongoing problem with theoretical descriptions of the Earth's atmosphere is a dichotomy in the representation of turbulent transport, between the turbulence estimated in weather forecast models, and the turbulence required for accurate simulations in air-quality forecast models. Representations of atmospheric turbulence used in weather forecast and climate models have focused on parameterizations of "sub-gridscale turbulence"; descriptions of the storage and release of energy derived from incoming solar radiation and anthropogenic heat release, physical factors in the built-environment, and the transfer of sensible and latent heat between the built environment and the atmosphere. These efforts adhere to an underlying concept of radiative-driven flow: heat transfer from the sun and/or anthropogenic sources being the source of energy behind

31 atmospheric motions. There has been considerable research focused on improving understanding radiative-driven flow in
32 urban areas (e.g. the advection and diffusion associated with buildings and street canyons (Mensink *et al.*, 2014), urban heat
33 island radiative transfer theory (Mason *et al.*, 2000), and in efforts to increase 3D model vertical and horizontal resolution in
34 order to better capture the physical environment (Leroyer et al, 2014). However, when these physical models of turbulence
35 are applied to problems involving the emissions, transport and chemistry of atmospheric pollutants, predicted surface
36 concentrations of emitted pollutants may be biased high, and concentrations aloft biased low, indicating the presence of missing
37 additional sources of atmospheric dispersion (Makar *et al.*, 2014; Kim *et al.*, 2015). Despite ongoing work to improve the
38 turbulence schemes in meteorological models (Makar *et al.*, 2014; Hu *et al.*, 2013; Klein *et al.*, 2014), computational predictive
39 models of atmospheric pollution typically make use of a constant "floor" or "cut-off" in the thermal turbulent transfer
40 coefficients provided by weather forecast models, sometimes with higher values of this cutoff over urban compared to rural
41 areas (Makar *et al.*, 2014), in an attempt to compensate for apparent insufficient vertical mixing of chemical tracers. The
42 turbulent mixing in these physical descriptions, while capable of reproducing observed meteorological conditions, do not
43 explain lower concentration observations of emitted atmospheric pollutants.
44 Large stack sources of pollutants provide a useful analogy in investigating a potential cause of this discrepancy. Emissions
45 from these sources occur at high temperatures, lofting their emitted mass high into the atmosphere as a result of buoyancy
46 effects. However, the physical size of the stacks (< 10 m diameter) is much smaller than the grid cell size used in regional
47 models (km to 10's of km). In order to capture the rapid vertical redistribution of emissions from large stacks, sub-grid-scale
48 parameterizations are used, in which buoyancy calculations are performed to determine plume heights, which are then used to
49 determine the distribution of freshly emitted pollutants (Briggs, 1975; Briggs, 1984; Gordon *et al.*, 2018; Akingunola *et al.*,
50 2018). For large stack emissions, these parameterizations account for the effect of the addition of energy (the hot exhaust gas)
51 on the local distribution of pollutants, and are essential in estimating initial vertical distribution of those pollutants.
52 In this work, we investigate the potential for another type of at-source energy to influence the vertical distribution of freshly
53 emitted pollutant concentrations: the addition of kinetic energy due to the displacement of air during the passage of vehicles
54 on roadways. Roadway observations in the 1970's showed that this transferred energy has a significant influence on the
55 transport of primary pollutants released from vehicle exhaust, with vehicle passage being associated with "a distinct bulge in
56 the high frequency range of the wind spectrum", "corresponding to eddy sizes on the order of a few metres" (Rao *et al.*, 1979).
57 The same work found that the variation in the concentration of non-reactive tracers could be attributed to wakes behind moving
58 vehicles. Subsequent theoretical development led to the creation of the roadway-scale models describing turbulence within a
59 few 10's of metres around and above roadways, in turn used to estimate the very local-level impact of vehicles on emitted
60 pollutant concentrations (Eskridge and Catalano, 1987). These models showed that near-roadway concentrations of emitted
61 pollutants were highly dependent on vehicle speed, with over a factor of two reduction in emission-normalized pollutant
62 concentrations being associated with an increase in vehicle speed from 20 to 100 km/hr (Eskridge *et al.*, 1991). With the
63 advent of portable, very high time resolution 3-D sonic anemometers, the turbulent kinetic energy of individual vehicles could
64 be measured directly, either aboard an instrumented trailer towed behind a vehicle (Rao et al., 2002), or through

instrumentation mounted aboard a laboratory following other vehicles in traffic (Gordon *et al.*, 2012; Miller *et al.*, 2018). However, the application of this information has been limited up to now to theoretical and computational models of the near-roadway environment and large eddy simulation models with horizontal domains of a few kilometers in extent.

Regional air-quality models also have vertical resolution in the 10's of metres near the surface, suggesting the potential for vehicle-induced turbulence (VIT) to influence turbulent mixing out of the lowest model layer(s). Here we demonstrate that this sub-grid-scale vertical transport process, which due to its highly localized spatial nature (over roadways), has a disproportionate impact on the vertical distribution and transport of freshly emitted chemical tracers. A comparable sub-grid-scale process which has a similar influence on pollutants are the emissions from large stacks noted above (Gordon *et al.*, 2018; Akingunola *et al.*, 2018). Accurate estimation of pollutant concentrations from the latter sources must take into account the at-source buoyancy and exit velocity of high-temperature exhaust to determine the vertical distribution of fresh emissions. Similarly, our work focusses on determining the local lofting of pollutants from and due to moving vehicles, in order to adequately represent the at-source vertical distribution of their emissions, on the larger scale.

The extent of the vertical influence of VIT varies depending on the configuration of vehicles on the roadway. From observations taken from a trailer following an isolated passenger van (Rao *et al.*, 2002), and large eddy simulation (LES) / computational fluid dynamics (CFD) models of individual vehicles (Kim *et al.*, 2011; Kim *et al.*, 2016a), the vertical distance over which VIT can be distinguished from the background for isolated, *individual* vehicles (i.e. the mixing length) is on the order of 2.5 to 5.13 m. However, as we show in Methods and Results, for observations of *ensembles* of vehicles in traffic (Gordon *et al.*, 2012; Miller *et al.*, 2018), and large eddy / computational fluid dynamics simulations of *ensembles* of vehicles (Kim *et al.*, 2016a; Woodward *et al.*, 2019; Zhang *et al.*, 2017), the mixing lengths associated with VIT are larger, on the order of 10's of m, to as much as 41 m. The vertical extent of the impacts of alternating low and high areas of surface roughness have been shown to create downwind internal boundary layers to even more significant heights in the atmosphere (e.g 300m, Bou-Zeid *et al.*, 2004, their Figure 12), suggesting that impacts into the lower boundary layer due to the alternating roughness elements (in our case, vehicles versus roadways) is not unreasonable. We also show in Methods that the impact of VIT within the context of an air-quality model is via changes to the vertical gradient of the thermal turbulent transfer coefficients; the gradient of the sum of the natural turbulence and VIT terms, allows VIT to influence vertical mixing, even when model vertical resolution is relatively coarse.

Large eddy simulation (LES) / computational fluid dynamics (CFD) models have shown the importance of VIT towards modifying local values of turbulent kinetic energy, as noted in the references above. However, these models require relatively small grid cell sizes compared to regional chemistry models (cm to tens of metres) and time steps to allow forward time stepping predictions of future meteorology and chemistry. These constraints in turn severely limit the size of the domain in which they can be applied, and the processing time for simulations for these reduced domains can be very high. For example, the FLUENT model was used by Kim et al (2016a) with an adaptive mesh with a minimum cell size of 1 cm, with a 100x20x20m domain, while Woodward et al (2019)'s implementation of FLUENT had a cell size of 50 cm, operating in a domain of 600,000 nodes (a volume of 75,000 cubic metres), and an adaptive time step limited by a Courant number of 5. The

99 latter criteria implies a computation timestep of less than 0.09 s for a 100 km hr^{-1} vehicle (or wind) speed, while a 1 cm grid
100 cell size implies a computation timestep of less than 1.8×10^{-3} s timestep. Similarly, the LES model employed by Zhang et al
101 (2017) utilized a 1m x 2m x 1m cell size and a computation timestep of 0.03 s. Other LES models have larger horizontal
102 resolution, but are limited in horizontal domain extent relative to regional chemical transport models (example LES models
103 incorporating gas-phase chemistry include: Vinuesa and Vil.-Guerau de Arellano (2005), with a 50m horizontal resolution,
104 3.2x3.2 km domain), Ouwersloot et al. (2011), with a 50m horizontal resolution and a 12.8km x 12.8 km domain, Li et al.
105 (2016), with a 150m horizontal resolution and a 14.4km x 14.4km horizontal domain, and Kim *et al.* (2016b), with a 66.6m
106 horizontal resolution and a 6.4x6.4 km domain. In contrast, a 3D regional chemical transport model typically operates over a
107 domain with may be continental in extent (the simulations described here have a 10km and 2.5km horizontal resolutions with
108 7680x6380 km and 1300x1050km domains, respectively). The limiting horizontal resolution for regional chemical transport
109 models is on the order of kilometres, with a limiting vertical resolution on the order of 10's of metres, and timesteps on the
110 order of 1 minute. These limits for regional chemical transport models are a function of the need to provide chemical forecasts
111 over a relatively large region, within a reasonable amount of current supercomputer processing time (the chemical calculations
112 typically taking up the bulk of the processing time). LES models are capable of capturing VIT effects (Kim et al. (2016a),
113 Zhang et al., (2017), Woodward et al. (2019)), and their results have been used here in developing our parameterization, but
114 are constrained by current computer capacity from being applied for the larger scale domains required in regional to
115 continental-scale air pollution simulations. A "scale gap" exists between LES and regional chemical transport models – for
116 regional chemical transport models, parameterizations of the physical processes such as VIT, resolvable at the high resolution
117 of LES models, are therefore required. In return, these parameterizations allow the relative impact of the parameterized
118 processes on the larger domain sizes of regional chemical transport models to be determined.

119 **2 Methodology**

120 **2.1 Theoretical development**

121 In contrast to the very local resolution "roadway" models used to examine the impact of vehicle motion on pollutant
122 concentration (Eskridge and Catalano, 1987; Eskridge *et al.*, 1991), and computational fluid dynamics modelling of vehicle
123 turbulence (Kim *et al.*, 2011; Kim *et al.*, 2016a; Woodward *et al.*, 2019; Zhang *et al.*, 2017), 3D models of atmospheric
124 pollution (Galmarini *et al.*, 2015) have horizontal grid-cell sizes of a one to 10's of km, and thus emissions and vertical
125 transport associated with roadways must be approached from the standpoint of sub-grid-scale parameterizations.
126 Measurements of the turbulent kinetic energy (TKE) associated with vehicles are usually available on a "per-vehicle" or "per-
127 vehicle within an ensemble" basis. These observations provide the average on-road TKE per vehicle passing a point per unit
128 time (Gordon *et al.*, 2012; Miller *et al.*, 2018) and/or the shape of the enhanced TKE cross-section in the plane perpendicular
129 to the vehicle's motion (Rao *et al.*, 2002). A sub-gridscale parameterization linking these scales is therefore necessary in
130 order to study the impacts of VIT on the vertical redistribution of freshly emitted pollutants, and hence on large-scale

131 atmospheric chemistry and transport. Sub-gridscale parameterizations are commonly used in atmospheric models of weather

132 forecasting to provide the rates of change of processes which occur at scales smaller than the model's horizontal and/or vertical

133 resolution: cloud formation and buoyant plume rise from large stacks being a common example for model grid cell sizes of

134 10km or more (Kain, 2004; Briggs, 1975; Briggs 1984; Gordon *et al.*, 2018; Akingunola *et al.*, 2018).

135 Three separate problems must be addressed in the construction of such a VIT parameterization for atmospheric chemical

136 transport models, specifically:

137 (1)   What is the relationship governing the decrease in VIT with increasing distance (height) from the vehicles?

138 (2)   How can observation data, in units of vehicles per unit time, be related to variables more commonly available for

139 regional chemical transport models?

140 (3)   How can VIT be incorporated into a regional model in a manner that only the emissions due to vehicles are affected,

141 given that the vehicle-induced turbulence will have the most significant impact on emissions from moving vehicles due to the

142 relatively low area fraction of roadway area within a given grid cell?

143 We address each of these issues in the sub-sections that follow.

2.2 Changes in VIT with Height

145 Measurements of TKE behind a passenger van (Rao *et al.*, 2002) typically show a smooth distribution, with TKE decreasing

146 both above and below the height of the upper trailing edge of the moving vehicle. Similar results have been seen from very

147 high resolution computational fluid dynamics modelling of the flow around individual vehicles, though the shape of the vehicle

148 and the arrangement of vehicles on the roadway can have a strong influence on the location of the maximum and shape of the

149 vertical profile in TKE (Kim *et al.*, 2011; Kim *et al.*, 2016a). We examined four datasets (the observations of Rao *et al.*, 2002,

150 and the LES modelling of Kim *et al.*, 2016a; Woodward *et al.*, 2019; Zhang *et al.*, 2017) to evaluate the extent to which a

151 Gaussian distribution may be used to represent the decrease in VIT with height above moving vehicles, as well as examining

152 the expected range of mixing lengths which may result from VIT. A Gaussian distribution of TKE with height is given by

153 equation (1), where $I_q(z)$ is the time integrated added TKE value for vehicle type q with height z (m^2s^{-1}), h_q is the height of the

154 vehicle, and A_q and σ_q are numerical constants:

$$I_q(z) = \frac{A_q}{\sqrt{2\,\pi\,\sigma_q^2}} e^{\left(-\frac{(z-h_q)^2}{2\,\sigma_q^2}\right)} \tag{1}$$

156 Equation (1) may be re-written as:

$$ln\left(\sqrt{2\,\pi}\,I_q(z)\right) = ln\left(\frac{A_q}{\sigma_q}\right) - \frac{(z-h_q)^2}{2\,\sigma_q^2} \tag{2}$$

158 Equation (2) shows that values of $-(z-h_q)^2$ versus $ln\left(\sqrt{2\,\pi}\,I_q(z)\right)$, with the values of z taken from vertical profiles of $I_q(z)$

159 in the literature, will yield a slope of $\frac{1}{2\,\sigma_q^2}$ and an intercept of $ln\left(\frac{A_q}{\sigma_q}\right)$, and the correlation coefficient for this relationship may

160 be used to judge the accuracy of the use of a Gaussian distribution to describe the decrease in TKE with height above moving

161 vehicles. The resulting relationships may also be used to describe the vertical mixing length, defined "as the diameter of the

162 masses of fluid moving as a whole in each individual case; or again, as the distance traversed by a mass of this type before it

163 becomes blended in with neighbouring masses" (Prandtl, 1925; Bradshaw, 1974). Here we assume that this blending has

164 occurred at the height at which the Gaussian has dropped to 0.01 of the value at $z=h_q$ (i.e. the value of z at which VIT has

165 reached 1% of its maximum value (i.e. $e^{\left(-\frac{(z-h_q)^2}{2\,\sigma_q^2}\right)} = 0.01$).

166 An example of the analysis used to construct Table 1 appears in Figure 1, for a CFD example for an ensemble of vehicles,

167 taken from the literature (Kim *et al.*, 2016a). In this figure, contours of TKE are shown as solid lines. TKE values as a function

168 of height at three locations behind the trucks were used to determine σ_q and hence estimate the length scale via equations (1)

169 and (2). A notable feature of this example is the substantial increase in length scale which occurs between the initial vehicle

170 (a transport truck) and subsequent downwind vehicles (compare height of TKE contours, and the resulting length scales in

171 Figure 1, between left and right sides of the figure). Increases in downwind turbulent length scales associated with vehicles

172 moving in close ensembles are a common feature in the literature.

173

174 This analysis (see Table 1) shows that a Gaussian distribution accounts for much of the variability in TKE with height

175 (correlation coefficients of 0.54 to 0.99), and under realistic traffic conditions, the mixing lengths increase in size, and may be

176 considerably larger than those of isolated vehicles.

177 Two VIT mobile laboratory studies (Gordon *et al.*, 2012; Miller *et al.*, 2018) observed vehicle-per-second TKE for vehicles

178 moving in ensembles along multilane roadways, aggregated by vehicle classes using the same methodology, to derive formulae

179 for the net TKE added by VIT at 4m and 2m (the height of the instrumentation used in these studies). We combine these data

180 here to determine the change in VIT with height. Setting E as the TKE added due to the vehicles, two formulae result:

181
$$E(4m) = 1.8\,F_c + 2.2\,F_m + 20.4\,F_t$$
$$E(2m) = 2.4\,F_c + 6.2\,F_m + 14.8\,F_t$$
(3)

182 Where $E(4m)$ and $E(2m)$ are the TKE added driving within the ensemble at 4 and 2 m elevation from these two studies (m^2 s$^-$

183 ^{2}), and F_c, F_m, and F_t are the number of passenger cars, mid-sized (vans, flatbed pickup trucks, and SUVs) and large vehicles

184 (10 to 18 wheel heavy-duty vehicles) travelling past a given point on the highway per second. The numerical coefficients are

185 the time integrated TKE values (I_q) at the two heights (m^{2}s^{-1}). An alternative approach would be to make use of vehicle speed

186 data within each grid cell and parameterizations utilizing vehicle speed (Di Sabatino *et al.*, 2003; Kastner-Klein *et al.*, 2003)

187 to construct TKE additions due to the sub-grid-scale roadways. However, vehicle speed information is not currently readily

188 available on a gridded hourly basis, while estimates of vehicle km travelled are available in gridded form due to their use in

189 emissions processing, and making the simple scaling assumption that the vehicles travel across one dimension of a grid cell

190 allows us to generate the F_c values required to estimate TKE. Note that vehicle speed is implicit in this methodology utilizing

191 VKT – higher speeds will result in a greater number of vehicle km travelled per unit time, and hence higher TKE values. As

192 in the above discussion, we assume a Gaussian distribution of the coefficients of the TKE equations of (3) with height for each

193   vehicle, where h_q = 1.5m, 1.9m and 4.11m for cars, mid-sized vehicles and trucks, respectively, with each of the 2m and 4m

194   values of the coefficients of (3) being used to determine the corresponding values of A_q and σ_q of equation (1), (i.e. $q = c,m,t$).

195   The resulting height-dependent formulae may be used to replace the coefficients of (3), leading to the following formula for

196   the net turbulent kinetic energy associated with the number of vehicles in transit along a given stretch of roadway at a given

197   time:

$$
\begin{aligned}
E_{net}(z) = \ & 2.43 F_c\, e^{[-2.40 x 10^{-2}(z-1.5)^2]} \\
& + 15.58 F_m\, e^{[-1.18 x 10^{-1}(z-1.9)^2]} \\
& + 20.43 F_t\, e^{[-3.61 x 10^{-2}(z-4.11)^2]}
\end{aligned}
\tag{4}
$$

198

199   Most 3-D chemical transport models make use of some variation of "K-theory" diffusion to link turbulent kinetic energy to

200   mixing, with the vertical mixing of a transported variable c due to turbulence at heights z being related to the thermal turbulent

201   transfer coefficient K via:

$$
\frac{\partial c}{\partial t} = \frac{\partial}{\partial z}\left(K \frac{\partial c}{\partial z}\right)
\tag{5}
$$

202

203   Finite differences and tridiagonal matrix solvers are usually used to forward integrate equation (5). For example, the solver

204   used in the GEM-MACH model uses the following finite difference for the spatial derivatives (both spatial derivatives are

205   $O(\Delta\sigma^2)$, the derivatives are carried out in, and the K values are transformed into, $\sigma = \frac{P}{P_0}$ coordinates as $\widetilde{K}$, where P is the

206   pressure, and P_0 is the surface pressure):

$$
\frac{c_i^{n+1}-c_i^n}{\Delta t} = \frac{\frac{1}{2}(\widetilde{K}_{i+1}+\widetilde{K}_i)\left(\frac{c_{i+1}-c_i}{\sigma_{i+1}-\sigma_i}\right)-\frac{1}{2}(\widetilde{K}_i+\widetilde{K}_{i-1})\left(\frac{c_i-c_{i-1}}{\sigma_i-\sigma_{i-1}}\right)}{\sigma_{i+\frac{1}{2}}-\sigma_{i-\frac{1}{2}}}
\tag{6}
$$

207

208   Note in (6) that the prognostic values of K calculated by the weather forecast model are on the same vertical levels as

209   concentration; values of the additional component of K associated with VIT must therefore be calculated for model layers as

210   opposed to layer interfaces.

211   K and E may be linked through the relationship of Prandtl, where l is a characteristic length scale:

$$
K = 0.4\, l\sqrt{E}
\tag{7}
$$

212

213   As was done for Table 1, we have chosen this value on a per-vehicle basis as the vertical location at which the Gaussian

214   profiles derived above reach 0.01 (i.e. 1%) of their maximum value. Using each of the coefficient values of (3) at the two

215   heights, in conjunction with equation (1) treated as a two-variable in two unknowns (A_q, σ_q) problem we find values of l_c, l_m,

216   and l_t of 13.56, 6.25, and 11.28 m, respectively. These values are based on observed traffic conditions, and fall well within

217   the range of mixing lengths provided for vehicle ensembles in Table 1, however, we note that they are a source of uncertainty,

218   with the percent uncertainties (Gordon $et\ al.$, 2012) associated with the 4m values at ±52%, ±157%, and ±12% for cars, mid-

219   sized vehicles and trucks, respectively. The relatively low values of l_m and high uncertainties in the corresponding mid-sized

220   vehicle per-vehicle estimates of TKE relative to the other vehicle types are likely the result of a combination of small sample

221   size (Gordon $et\ al.$ (2012) noted the relative proportion of the three vehicle classes as 89.9% cars, 4.8% mid-sized, and 5.3%

222   trucks, respectively) and the variety of ensemble versus isolated vehicles sampled (noting the variation in Table 1 for vehicles

223 within the smaller vehicle size classes). Additional observations of vehicle turbulence are clearly needed, particularly in the

224 region above the largest vehicles on the road (4.1m), using remote sensing techniques such as Doppler lidar, in order to improve

225 mixing length estimates. However, the values used here are reasonable with respect to the available data, and while likely

226 overestimating the mixing length associated with isolated vehicles (Rao *et al.*, 2002; Kim *et al.*, 2016a) likely underestimate

227 the mixing length of ensembles of vehicles (Kim *et al.*, 2016a), particularly for ensembles moving within street canyons

228 (Woodward *et al.*, 2019; Zhang *et al.*, 2017). The latter represent the some of the specific regions where vehicle emissions are

229 likely to dominate.

230 We derive the following formula for the addition to the thermal turbulent transfer coefficient associated with vehicle passage

231 as a function of height:

232
$$K_{VIT}(z) = 0.4 \frac{l_c F_c + l_m F_m + l_t F_t}{F_c + F_m + F_t} \sqrt{\left\{ \begin{array}{l} 2.43 F_c e^{[-2.40 \times 10^{-2}(z-1.5)^2]} \\ +15.58 F_m e^{[-1.18 \times 10^{-1}(z-1.9)^2]} \\ +20.43 F_t e^{[-3.61 \times 10^{-2}(z-4.11)^2]} \end{array} \right\}} \tag{8}$$

233

234 The use of (8) must be undertaken with care. Like most regional air-quality models, the vertical resolution of GEM-MACH

235 used here is relatively coarse (the first four model layer midpoints are located approximately 24.9, 99.8, 205.0, and 327.0 m

236 above the surface). Layer midpoint values must be representative of the layer resolution in order to describe the impact of

237 VIT on the layer. A simple linear interpolation between the peak values of K_{VIT} and the first model interface will overestimate

238 the impact of VIT within the lowest model layer, while the use of (8) for the mid-point value alone will underestimate the

239 influence of VIT within the lowest part of the first model layer. The best representation of a sub-grid-scale scalar quantity

240 within a discrete model layer is its vertical average within that layer. Here, we calculate the vertically integrated average of

241 (8) within each model layer, to provide the best estimate of the impact of VIT, to within the vertical resolution of the model.

242 **2.3 VIT and Model Vertical Resolution**

243 The issue of the vertical extent of the impact of VIT is worth considering in the context of model layer thickness. Given that

244 the vertical length scale of added VIT is on the order of 10's of metres, as denoted in the studies quoted herein, it is reasonable

245 to question whether the added turbulence should be expected to have an impact on the dispersion of pollutants. This apparent

246 contradiction is easily resolved by noting, (1) that the turbulence due to VIT is added as an addition to the pre-existing

247 "meteorological" thermal turbulent transfer coefficient (with the *net* turbulence profile, not the VIT alone, determining its

248 impact on vertical mixing); and (2) that the impact of this net turbulence does not depend just on the magnitude of the net

249 coefficients of thermal turbulent transfer, but also on their vertical gradient. This second point can be illustrated by expanding

250 the diffusion equation using the chain run of calculus (i.e. $\frac{\partial c}{\partial t} = \frac{\partial}{\partial z}\left(K_{net}\frac{\partial c}{\partial z}\right) = K_{net}\frac{\partial^2 c}{\partial z^2} + \frac{\partial K_{net}}{\partial z}\frac{\partial c}{\partial z}$), and the aid of an example,

251 shown in Figure 2. Figure 2 displays examples of cases where the concentration gradient and natural thermal turbulent transfer

252 coefficient both decrease linearly with height (Figure 2(a,b)), and where the concentration gradient decreases with height while

253 the natural thermal turbulent transfer coefficients increase with height (Figure 2(c,d)). The added K_{VIT} is shown as a blue

254 dashed line, and the net vertical thermal turbulent transfer is shown as a red line. Figure 2 (a) and Figure 2(c) depict these

255 curves at a high vertical resolution, while Figure 2(b) and Figure 2(d) depict them at a low (regional model) resolution. Note

256 that in the latter, the vehicle-induced addition to the net thermal turbulent transfer coefficient depicted in Figure 2(a,c) lies

257 entirely within the lowest model layer of Figure 2(b,d). In both Figure 2(a) and Figure 2(b), the impact of K_{VIT} is to slow the

258 build-up of near-surface concentrations. In both Figure 2(c) and Figure 2(d), the impact of K_{VIT} is to more rapidly vent near-

259 surface concentrations further up into the atmosphere. That is, at both high and low resolution, K_{VIT} affects near-surface

260 concentrations, due to the vertical gradient of $\frac{\partial K_{net}}{\partial z}$). Centered difference calculations for the low resolution case are shown

261 in Figure 2(b,d) to illustrate the point that gradients in low vertical resolution net diffusivity result in reductions in lowest

262 model layer trapping, and increases in venting from this lowest layer. In both of these cases, the addition of vehicle turbulence

263 to the lowest model layer changes the gradient of the net thermal turbulent transfer coefficient, in turn leading to reduced

264 surface concentrations. The above example illustrates the manner in which VIT may have an impact even on relatively low

265 vertical model resolution.

266 2.4 Relating VIT to Available Gridded Data – Vehicle Km Travelled

267 Along individual roadways, equation (8) makes use of F_c, F_m, and F_t observations at points along roadways within a grid-cell,

268 hence deriving local estimates of VIT. This data is currently difficult to obtain for large-scale applications, and hence we

269 have turned to secondary sources of information to estimate these three terms. Vehicle Kilometer Travelled (VKT) is used for

270 estimating on-road vehicle emissions at jurisdiction level (e.g. county level for the US and province level for Canada) for

271 national emissions inventories. Emissions processing systems used for air-quality models make use of spatial surrogates to

272 help determine the spatial allocation of the mass emitted from different types of vehicles on different roadways (Adelman *et*

273 *al.*, 2017). The same set of surrogates is used for calculating VKT (km s^{-1}) for each grid cell of the model domain (varying

274 by hour of day and day of week, for each of the three vehicle categories listed (see Figure 3), in turn providing diurnal variations

275 of VIT matching traffic flow. The data shown are derived from 2006 Canadian (Taylor, 2019) and 2011-based projected 2017

276 US VKT (EPA, 2017). Note that for the 10km grid cell size used here, values of F_c, F_m, and F_t may be derived by dividing

277 these numbers by 10. The largest contribution to total vehicle km travelled is by the "cars" class (Figure 3(a)) due to their

278 greater numbers (the originating study (Miller *et al.*, 2018) found that 89.9% of vehicles measured were cars), followed by

279 trucks (Figure 3(c); 5.3% of vehicles measured), and mid-sized vehicles (Figure 3(b); 4.8% of vehicles measured).

280 These VKT data may be linked to the above VIT formula (8), provided the distance each vehicle is travelling within that grid

281 cell is known. Here, we have made two additional assumptions. The first assumption is that each vehicle carries out a simple

282 transit of the cell – the distance travelled is the cell-size. While this may be a reasonable first-order approximation, we note

283 that it has limitations: for example, when the number of vehicles on the roads overwhelm the capacity of the roads (rush-hour

284 traffic jams) the distance travelled decreases. However, under these circumstances the VKT values will also decrease; the

285 impact of rush-hour conditions should to some extent be included within the VKT estimates available for emissions processing
286 systems. The second assumption is that the VKT contributions within a grid-cell are additive – i.e. that their numbers may be
287 added via the "F" terms in (8) (Gordon *et al.*, 2012; Miller *et al.*, 2018), an assumption found to be accurate in CFD modelling
288 (Kim *et al.*, 2016a). Note that this assumption may result in overestimates of the net TKE – a better methodology for future
289 work would be to collect and make use of statistics of vehicle density by roadway type within each grid-cell. However, we
290 note that assuming that vehicles are evenly distributed over roadways in a grid cell would result in a net underestimate of the
291 TKE contributed over the larger roadways and main arteries of urban areas.

292 Example 10 AM EDT North American 10km resolution gridded vehicle-induced thermal turbulent transfer coefficient values
293 (K_{VIT}, equation 8) created using these assumptions, and an example vertical profile of K_{VIT} for central Manhattan Island at
294 0.5m vertical resolution are shown in Figure 4. The resulting enhancements to "natural" K values at the vertical resolution of
295 the version of the GEM-MACH air-quality model, at 2.5km horizontal resolution, are shown in Figure S1 as dashed lines. The
296 enhancements are confined to the lowest model layer, as might be expected from the vertical resolution employed in this
297 version of GEM-MACH. Nevertheless, the values are sufficient to significantly change simulated vertical transport due to
298 modifications to the resolved gradient in thermal turbulent transfer coefficients, as discussed above. Both the magnitude and
299 gradient of $K_{net} = K + K_{VIT}$ may contribute to the concentration changes: breaking the vertical diffusion equation down using
300 the chain rule, (5) may be rewritten

301
$$\frac{\partial c}{\partial t} = K \frac{\partial^2 c}{\partial z^2} + \frac{\partial K}{\partial z} \frac{\partial c}{\partial z} \tag{9}$$

302 Both terms on the right-hand-side of (9) may contribute to decreases in concentration c at the surface and increases in
303 concentrations aloft. If the near-surface concentration profile ($\partial c/\partial z$) is negative (concentrations decrease with height), then
304 increases in K will result in surface concentration decreases). If this results in sufficient lofting that the concentration profile
305 maximizes above the ground (i.e. $\partial c/\partial z$ becomes positive near the surface), then decreasing values of K with height (i.e.
306 negative values of $\partial K/\partial z$) will also result in a shift towards negative rates of change, through the second term in the right-hand-
307 side of (9). All six panels of Figure S1 show increased *K* values; i.e. increases in the first term in (9). All six panels also
308 show a trend of $\partial K/\partial z$ becoming more negative (that is, near-surface positive slopes become less positive, negative slopes
309 become more negative), decreasing the magnitude of the second term in (9) in Figure S1 (b,c,d,f), and switching to a negative
310 rate of change in Figure S1(a,e). Both changes in the magnitude and gradient of *K* resulting from VIT contribute to the resulting
311 changes in surface concentration.

312 The thermal turbulent transfer coefficient values of Figure S1 may also be compared to the minima on "natural" K values
313 imposed in air pollution models in an attempt to account for missing subgrid-scale mixing (Makar *et al.*, 2014; these are
314 typically on the order of 0.1 to 2.0 $m^2 s^{-1}$). Aside from Figure S1(a), the vertical profiles here would not be modified by these
315 lower limits. We also note that these VIT-induced changes in total thermal turbulent transfer coefficients only impact the
316 species emitted at the road-way level, as discussed below.

2.5 Construction of a Sub-Gridscale Parameterization for On-Road Vehicle-Induced Turbulence

We note that the portion of the area of a grid-cell which is roadway-covered will be relatively small for most air pollution model resolutions, such as those considered here. For example, satellite imagery of the largest freeways show these to have a width of less than 400m. Hence, the largest roads make up less than 1/5 of the total area of a 2.5km grid-cell, and less than 1/20 of a 10km grid cell). The largest impact of VIT is thus likely to be for the chemical species being emitted by the mobile sources, in terms of the grid-cell average concentration. Furthermore, the grid cell approach common to these models results in horizontal numerical diffusion from the roadway scale to the grid cell scale: sub-grid-cell scale emissions are automatically mixed across the extent of the grid cell. The key impact of VIT will thus be in the vertical dispersion of the pollutants emitted from mobile sources. We must therefore devise a numerical means to ensure this additional source of diffusion is added to the model, bearing these constraints in mind.

Two examples of similar sub-gridscale processes appear in the literature. The first example are the cloud convection parameterizations used in numerical weather forecast models (Kain *et al.*, 2004), wherein the formation and vertical transport associated with convective clouds, are known to occur at smaller scales than the grid cell size employed in a numerical weather prediction model, are treated using sub-gridscale parameterizations. In these parameterizations, cloud formation and transport are calculated within the grid-cell on a statistical basis, using formulae linking the local processes to the resolvable scale of the model. The second example is found in the treatment of emissions from large stacks within air-quality forecast models (Gordon *et al.*, 2018; Akingunola *et al.*, 2018). These sources usually have stack diameters on the order less than 10m, and these sources emit large amounts of pollutant mass at high temperatures and velocities. In order to represent these sources, the most common approach is to calculate the height of the buoyant plume using the predicted ambient meteorology (vertical temperature profile, etc.) as well as the stack parameters (exit velocity, exit temperature, stack diameter). The emitted mass during the model timestep from the stack is then distributed over a defined vertical region within the gridcell in which the source resides. Note that the mass is also automatically distributed immediately in the horizontal dimension within the grid cell – the key issue is to ensure that the emitted mass is properly distributed in the vertical dimension. Our aim in the VIT parameterization that follows is identical in intent to that of the existing major point source treatments in air-quality models: to redistribute the mass emitted by vehicle sources in the vertical dimension, taking the very local physics influencing that vertical transport of fresh emissions into account. We therefore focus on determining the at-source vertical transport of emitted mass associated with VIT.

We start with the formulae for the transport of chemical species by vertical diffusion:

$$\frac{\partial c_i}{\partial t} = \frac{\partial}{\partial z}\left(K\frac{\partial c_i}{\partial z}\right) + E_i \tag{10}$$

Where c_i is the emitted chemical species, K represents the sum of all forms of thermal turbulent transfer in the grid-cell, and E_i is the emissions source term for the species emitted at the surface (applied as a lower boundary condition on the diffusion equation). For grid-cells containing roadways and hence mobile emissions, we split K into meteorological and vehicle-induced

349 components (K_T and K_{VIT} respectively), and the emissions into those from mobile sources and those from all other sources

350 ($E_{i,mob}$ and $E_{i,oth}$, respectively):

$$\frac{\partial c_i}{\partial t} = \frac{\partial}{\partial z}\left[(K_T + K_{VIT})\frac{\partial c_i}{\partial z}\right] + E_{i,mob} + E_{i,oth} \tag{11}$$

352 The terms in (11) may be rearranged:

$$\frac{\partial c_i}{\partial t} = \left\{\frac{\partial}{\partial z}\left[K_T \frac{\partial c_i}{\partial z}\right] + E_{i,oth}\right\} + \left\{\frac{\partial}{\partial z}\left[(K_T + K_{VIT})\frac{\partial c_i}{\partial z}\right] + E_{i,mob}\right\} - \left\{\frac{\partial}{\partial z}\left[K_T \frac{\partial c_i}{\partial z}\right]\right\} \tag{12}$$

354

355 The first bracketed term in (12) describes the rate of change of the chemical due to its emission by non-mobile area sources

356 and vertical diffusion due to meteorological sources of turbulence within the grid-cell, but outside of the sub-grid-scale

357 roadway. The second term describes the rate of change of the vertical diffusion of the mobile-source-emitted pollutants over

358 the sub-grid-cell roadway, which experiences both meteorological and roadway turbulence, and the final term prevents double-

359 counting of the meteorological component in equation (11), which is equivalent to equation (12). Note that turbulent mixing

360 for non-emitted chemicals is determined by solving equation (5), and for chemicals which are not emitted from mobile on-

361 road sources, equation (10) is solved, with $E_i = E_{i,oth}$. This form of the diffusion equation (12) allows the net change in

362 concentration to be calculated from three successive calls of the diffusion solver, starting from the same initial concentration

363 field. One advantage of this approach is that existing code modules for the solution of the vertical diffusion equation may be

364 used – rather than being used once, they are used three times, with different values for the input coefficients of thermal turbulent

365 transfer coefficient (K) and for the lower boundary conditions (E).. The solution, once a suitable means of estimating K_{VIT} is

366 available, is thus relatively easy to implement in existing numerical air pollution model frameworks.

367 **2.6 Comparison of energy densities: VIT, Solar, and Urban Perturbations in Sensible and Latent Heat**

368 The relative contribution of TKE from VIT towards energy density can be compared to the daytime solar maximum energy

369 input to illustrate why VKT has relatively little impact during daylight hours, particularly in the summer. The maximum TKE

370 from VIT can be determined easily from Figure 3 and the use of our formulae; Figure 3(a) shows vehicle km travelled values

371 ranging from a maximum of 308 in the highest density 10km grid cell in North America (New York City) down through four

372 orders of magnitude in background grid cells with few vehicles. A typical urban value would be 30.8 VKT: this gives an F_c

373 value from our formulae of 3.08 vehicles s^{-1} for a 10km grid cell size. Assuming that the vehicles are all cars, from our

374 formulae we have a corresponding total TKE added at the point crossed by the vehicles, at height z=h$_{cars}$=1.5 m, of 7.48 m^2 s^{-2}.

375 We can combine this and the F_c value along with the area and volume of a lane of a roadway to estimate the energy density

376 (E_{VIT}) on dimensional grounds:

$$E_{VIT} = \left[\frac{(TKE)(air\ density)(lane\ volume)F_c}{(lane\ area)}\right] \tag{13}$$

378 Assuming each vehicle has a length of 4.5 m, width of 2.0 m, height of 1.5m, a lane length of 10 km, and an air density of

379 1.225 kg m^{-3}, one arrives at 84.8 kg s^{-3}, and values ranging from a North American grid maximum of 848 kg s^{-3} to a background

380 value four orders of magnitude smaller (8.48x10^{-2} kg s^{-3}). These energy densities may be compared to the typical solar energy

381 density reaching the surface at mid-latitudes of 1300 W m^{-2}, or in SI units, 1300 kg s^{-3}, and the typical range of perturbations

382 in latent and sensible heat fluxes associated with the use of a more complex urban radiative transfer scheme (the Town Energy

383 Balance module; Mason, 2000) in our 2.5km grid cell size simulations (typical diurnal ranges in the perturbations associated

384 with/without use of TEB: latent: -200 to +3 W m^{-2}; sensible: -100 to +100 W m^{-2} respectively). That is, under most daylight

385 conditions, the energy densities associated with VIT will be relatively small compared to the solar energy density at midday,

386 with a typical urban value of 6.5%, and range from 65% in the cell with the highest VKT values down to 0.0065% in

387 background conditions where the vehicle numbers are relatively small. Urban traffic however may contribute similar energy

388 levels as the changes in net latent and sensible heat fluxes associated with the use of an urban canopy radiative transfer model.

389 We also note that at night, during the low sun angle conditions of early dawn late evening, and during the lower sun angles of

390 winter, the relative importance of VIT to solar radiative input will be larger. Consequently, the impact of VIT will be higher

391 at night and in the early morning rush hours, and at other times when the sun is down or sun angles are low, as is demonstrated

392 below.

393 **2.7 GEM-MACH simulations**

394 A research version of the Global Environmental Multiscale – Modelling Air-quality and CHemistry (GEM-MACH) numerical

395 air quality model, based on version 2.0.3 of the GEM-MACH platform, was used for the simulations carried out here (Makar

396 *et al.*, 2017; Moran *et al.*, 2010; Moran *et al.*, 2018; Chen *et al.*, 2020). GEM-MACH is a comprehensive 3D deterministic

397 predictive numerical transport model, with process modules for gas and aqueous phase chemistry, inorganic particle

398 thermodynamics, secondary organic aerosol formation, vertical diffusion (in which area sources such as vehicle emissions are

399 treated as lower boundary conditions on the vertical diffusion equation), advective transport, and particle microphysics and

400 deposition. The model makes use of a sectional approach for the aerosol size distribution, here employing 12 aerosol bins.

401 The version used here also follows the "fully coupled" paradigm – the aerosols formed in the model's chemical modules in

402 turn may modify the model's meteorology via the direct and indirect effects (Makar *et al.*, 2015a,b; Makar *et al.*, 2017). The

403 meteorological model forming the basis of the simulations carried out here is version 4.9.8 of the Global Environmental

404 Multiscale weather forecast model (Cote *et al.*, 1998a,b; Caron *et al.*, 2015; Milbrandt *et al.*, 2016). Emissions for the

405 simulations conducted here were created from the most recent available inventories at the time the simulations were carried

406 out – the 2015 Canadian area and point source emissions inventory, 2013 Canadian transportation (onroad and offroad)

407 emissions inventory, and 2011-based projected 2017 US emissions inventory. As noted above, the model simulations were

408 carried out on two separate model domains shown in Figure 5; a 10 km horizontal grid cell size North American domain

409 (768x638 grid cells; 7680x6380 km), and a 2.5km horizontal grid cell size PanAm Games domain (520x420 grid cells;

410 1300x1050 km). For the 10km domain, simulations were for the month of July, 2016, while for the higher resolution model,

411 month-long summer (July 2015) and winter (January 2016) simulations were carried out, with and without the VIT

412 parameterization. These periods were based on the availability of emissions data, previous model simulations for the same

413 time periods appearing in the literature (Makar *et al.*, 2017; Stroud *et al.*, 2020), and the timing of a prior field study (Stroud
414 *et al.*, 2020).

2.8 VIT as a Sub-grid-scale Phenomena

416 It should be noted that the VIT enhancements to turbulent exchange coefficients are used to determine the vertical distribution
417 of freshly emitted pollutants at each model time step – they are not applied for all species within a model grid cell. Similar
418 sub-grid-scale approaches are used for the vertical redistribution of mass from large stack sources of pollutants, where
419 buoyancy calculations are applied to determine the rise and vertical distribution of pollutants from large industrial sources.
420 Both stacks and roadways are treated as sub-grid-scale sources of pollutants which are influenced by very local sources of
421 energy (stacks: high emission temperatures and exit velocities; roadways: vehicle induced turbulence) resulting in an enhanced
422 vertical redistribution of newly emitted chemical species. In both cases, the vertical transport results from an interplay between
423 the energy associated with the emission process (stacks: high temperature emissions with the ambient vertical temperature
424 profile; VIT: kinetic energy imparted to the atmosphere in which emissions have been injected with the ambient turbulent
425 kinetic energy). This interaction precludes a treatment solely from the standpoint of model input emissions, since the extent
426 of the mixing will depend on the local atmospheric conditions as well as the energy added due to the manner in which the
427 emissions occur. Both processes have been addressed by large eddy simulation modelling on a very local scale, but
428 parameterizations are required in both cases for regional scale simulations. In both cases, the parameterized vertical
429 redistribution of pollutants is applied to freshly emitted species – the horizontal spatial extent of the emitting region is
430 sufficiently small that although present, the enhanced mixing will have a minor effect on the redistribution of pre-existing
431 chemicals and on other atmospheric constituents affected by vertical transport. VIT in the context of regional chemical
432 transport models is thus best treated as a sub-grid-scale phenomena applied to fresh emissions, in direct analogy to the approach
433 taken for large stack emissions.
434

3 Results

3.1 VIT Height Dependence as a Gaussian Distribution

437 Under Methods, we describe the potential for the use of a Gaussian distribution to describe the fall-off in TKE with height
438 above vehicles. Using the equations presented there, we have analyzed VIT studies appearing in the literature, determining
439 the decrease in TKE as a function of height from published figures, then fitting these data to a Gaussian distribution to the
440 height above ground. The result of this analysis for several data sets is shown in Table 1, generated by extracting vehicle
441 centerline TKE values from contour plots of published data, and is subdivided into isolated vehicle and vehicle ensemble
442 studies and cases.

443 The inferred mixing length shows a marked variation between that of isolated vehicles or the lead vehicle in an ensemble, and

444 that of other vehicles appearing further back in the ensemble. Both directly observed and CFD modelled values of the inferred

445 mixing length for *isolated* vehicles or the *lead* vehicles of an ensemble vary from 2.5 to 5.13 m. For subsequent vehicles in

446 an ensemble, the mixing lengths increase to range from 4.6 to 41m. The difference in mixing length between the lead vehicle

447 in an ensemble, and subsequent identical vehicles appearing later in the ensemble also increases. For example note that diesel

448 truck mixing lengths inferred from the CFD modelling examining different vehicle configurations (Kim *et al.*, 2016a) increase

449 from 5.13 to 14.64 m, and the mixing lengths for automobiles increase from 2.50 m (isolated automobile), to 4.6m (automobile

450 two vehicles back from a lead diesel truck), to 9.41 m (automobile immediately behind a leading diesel truck). The mixing

451 length associated with VIT may also be significantly influenced by the ambient wind and local built environment – the mixing

452 length associated with the component of TKE due to VIT within street canyons (Woodward *et al.*, 2019; Zhang *et al.*, 2017)

453 ranges from 2/3 to greater than the street canyon height, with maximum mixing lengths of 41m. It is important to note that

454 these mixing lengths are driven by the vehicle passage within the canyon; they result from the additional TKE added

455 with/without vehicles in the CFD simulations. The above data show that a Gaussian distribution provides a reasonable

456 description of the decrease of TKE from vehicles with height, and, under realistic traffic conditions, the mixing lengths increase

457 in size, and are be considerably larger than those of isolated vehicles, and are comparable to or greater than the near-surface

458 vertical discretization of air quality models.

459 The length scales associated with VIT range from 2.50 m in the case of isolated vehicles (Kim *et al.*, 2016a), through ~10 m

460 for vehicles moving in ensembles (Woodward *et al.*, 2019; Zhang *et al.*, 2017) up to 41 m, with the larger values being typical

461 for urban street canyons. The latter describe the specific regions VIT is expected to have the greatest impact, given the high

462 vehicle density within the urban core. However, our parameterization makes use of length scales derived from observations

463 on open (non-street canyon) freeways (Gordon *et al.* 2012; Miller *et al.*, 2018), and thus may underestimate the length scales

464 in the urban core. The impact of multiple vehicles travelling in an ensemble on open roadways was specifically depicted in

465 the open roadway simulations of Kim *et al.* (2016a) reproduced in Figure 1, where the vertical extent of turbulent mixing was

466 shown to grow with increasing number of vehicles travelling in an ensemble. Furthermore, as was discussed and demonstrated

467 in Methods using the diffusivity equation, the length scale of the turbulence need not be greater than the model lowest layer

468 resolution in order to capture the impacts of VIT on mixing, being due in part to the gradient in turbulence with height.

469 **3.2 Model Domains and Evaluation Data**

470 Our 3D air-quality model (GEM-MACH) and our VIT parameterization, including its diurnal variation, are described under

471 Methods. Two air-quality model grid cell size and domain configurations were used for our simulations – the first employs a

472 10km grid cell size with a North American domain, and is used for the current operational GEM-MACH air-quality forecast

473 (Moran *et al.*, 2010; Moran *et al.*, 2018; Figure 5(a)). The second was a 2.5km grid-cell resolution domain focused on the

474 region between southern Ontario, Quebec and northeastern USA (Joe *et al.*, 2018; Ren *et al.*, 2020; Stroud *et al.*, 2020; Figure

475 5(b)).

476 The impact of VIT was determined through paired model simulations, with and without the VIT parameterization, evaluated
477 against surface monitoring network data. The latter include hourly model output for ozone (O_3), nitrogen dioxide (NO_2), and
478 particulate matter with diameters less than 2.5 μm (PM2.5), across North America and in our high resolution eastern North
479 America domain, evaluated at observation station locations with data from the AirNow network (AirNow, 2020). Observation
480 station locations used in simulation evaluation for these species are shown in Figure 6, for the two model configurations. The
481 juxtaposition of observation stations with urban populations (where the highest vehicle density may be found) may be seen by
482 comparing Figure 6 with Figure S2.

3.3 Continental 10 km Grid Cell Size Domain Evaluation

484 Simulations were carried out for the month of July, 2016 for the 10km grid cell size North American domain. Model
485 performance metrics used to here are described in Table S1, and provided for the 10 km resolution "VIT" and "No VIT"
486 simulations relative to the hourly observation data for PM2.5, NO_2, and O_3 in Table 2. These three chemicals were chosen
487 due to their well-known link to human health impacts of air pollution (Steib *et al.*, 2008; Abelsohn *et al.*, 2011).
488 The addition of VIT improved the scores for most performance metrics (bold-face print in Table 2). For NO_2, the addition of
489 VIT improved all scores with the exception of the correlation coefficient, which was degraded in the third digit. All PM2.5
490 scores improved, with the exception of the mean bias, which became more negative by 0.5 μg m^{-3} across North America. All
491 ozone scores improved, the exceptions being the correlation coefficient (which was the same for both simulations, or improved
492 in the 3rd digit depending on the domain or country), and the ozone mean bias for the USA (which increased by +0.18 ppbv).
493 Some of the improvements were substantial, when considered in a relative sense: this was most noticeable for the NO_2 scores,
494 with the North American Mean Bias for NO_2 improving by a factor of 8.4, the mean gross error and index of agreement by
495 19%, the root mean square error by 25%, and the FAC2 score by 6%. Relative improvements for PM2.5 across North America
496 were more modest (ranging from 0.3% for FAC2 to 14% for the correlation coefficient. The corresponding relative changes
497 for O_3 ranged from a 22% reduction in the mean bias magnitude to a fraction of a percent improvement for FAC2, mean gross
498 error, root mean square error, and index of agreement. Overall, the model performance for the Continental 10km domain July
499 2016 simulations improved across different metrics, indicating that the increased vertical turbulent mixing resulting from the
500 incorporation of VIT results in a more accurate representation of atmospheric mixing and chemistry.
501 Following the above comparison using all available surface monitoring network data (Table 2), we carried out a further
502 evaluation where the stations were selected based on human population within grid cells (Figure S2(a)), with only those stations
503 in which the population exceeded 800 km^{-2} used for analysis. The results of this evaluation are shown in Table S2, which may
504 be compared to Table 2 to show the relative influence of VIT on high population areas. We note that the magnitude of the
505 improvement in model performance associated with VIT has increased for many statistics when high population (i.e. high
506 vehicle traffic) areas are examined separately in this manner; for example the incremental improvement in North American
507 NO_2 mean bias changes from 1.053 ppbv for all stations versus 1.782 for population > 800 km^{-2} stations, and the incremental
508 improvement in PM2.5 MGE for North America changes from 0.249 to 0.665 μg m^{-3} (both numbers are differences between

509 No VIT and VIT values in Tables 2 and S2 in each case. The number of model performance improvements with the use of

510 VIT has increased when grid cells with populations greater than 800 km^{-2} are evaluated (62 out of 72 metrics improved with

511 the use of VIT in Table 2, while 66 out of 72 metrics improved for stations corresponding to grid cells with populations greater

512 than 800 km^{-2}). Most of these additional improvements were associated with better ozone prediction performance in urban

513 regions.

514 The timing and spatial distribution of the differences in the 29 day mean values of NO$_2$, PM2.5 and O$_3$ at 10 and 22 UT (6 AM

515 and 6 PM EDT) are shown in Figure 7. NO$_2$ and PM2.5 have decreased in the urban areas and along the major road networks

516 in the early morning (Figure 7(a,c)), while the ozone (Figure 7(e)) increases in the urban areas and along the roadways, with a

517 minor increase in the surrounding countryside. The VIT effect occurs at night and in the early morning: the average differences

518 are minimal by 6 PM EDT (Figure 7 (b,d,f)). This diurnal cycle of the average impact of VIT is expected: at night and during

519 the early morning the radiative-transfer driven atmosphere is relatively stable, natural background turbulence is low in

520 magnitude, and the relative contribution of VIT is therefore large. The reverse is true during the later morning to late afternoon,

521 as the solar radiative balance causes near-surface turbulence to rise several orders of magnitude relative to nighttime values,

522 and the relative contribution of VIT at those times becomes minimal. The strongest contribution of VIT thus occurs under

523 more stable atmospheric conditions: at night and in the early morning.

524 The region over which the two simulations' mean values differ at the 90% confidence level is shown in Figure 8. The

525 difference between the mean values of the two simulations (M_{VIT}, M_{NoVIT}) becomes significant at a confidence level c if the

526 regions defined by $M_{VIT} \pm z^* \frac{\sigma_{VIT}}{\sqrt{N}}$ and $M_{NoVIT} \pm z^* \frac{\sigma_{NoVIT}}{\sqrt{N}}$ do not overlap (where N is the number of gridpoint values averaged,

527 the σ values are the standard deviations of the means, and z^* is the value of the $\sqrt{c}$ percentile point for the fractional confidence

528 interval c of the normal distribution, where $z^*=1.645$ at $c=0.90$. Grid cell values where the mean values differ at or above the

529 90% confidence level are thus defined as $\frac{|M_{VIT}-M_{NoVIT}|}{\frac{z^*}{\sqrt{N}}(\sigma_{VIT}+\sigma_{NoVIT})} > 1$ thus differ at greater than the 90% confidence level. The mean

530 values at each gridpoint and their standard deviations may thus be used to determine the confidence level – these values for

531 each of the mean differences of Figure 7 are shown in Figure 8, with red colours indicating differences significant at greater

532 than 90% confidence.

533 From Figure 8, it can be seen that the continental scale model means for the VIT versus No VIT simulations for surface NO$_2$,

534 surface PM2.5 and surface O$_3$ at night differ at 90% confidence, over much of the domain for NO$_2$ and PM2.5, and in urban

535 core areas for O$_3$. The spatial extent of 90% confidence is much greater under the stable conditions of night (Figure 8(a,c,e))

536 than the less stable conditions of daytime (Figure 8(b,d,f)), as would be expected from the relative magnitude of K$_T$ versus

537 K$_{VIT}$ during the day and night. While the nighttime influence of VIT on NO$_2$ extends over much of the continent, for O$_3$, the

538 impact is primarily within the cities, where the increased mixing of NOx results in higher nighttime O$_3$ concentrations due to

539 decreased NOx titration.

540 The all-domain model performance metrics of Table 2 were also calculated for each measurement station, and the appropriate

541 differences in the metrics or their absolute values were used to determine location-specific impacts of the VIT parameterization

542 for NO_2, PM2.5 and O_3 (Figures 9, S3 and S4). Differences in the values of the metrics between the two simulations are
543 shown, with the sign of the differences arranged so that red/blue colours indicate better performance for the VIT/No VIT
544 simulations respectively, red indicating better scores for the VIT simulation. The colour scales in these Figures are arranged
545 to include 3 orders of magnitude between lowest and highest difference scores and zero, and to encompass the maximum value
546 of the differences observed at across all stations. The values vary between metrics and the chemical species, with the largest
547 changes occurring for NO_2, followed by PM2.5 and the smallest changes for O_3, relative to typical concentrations of these
548 species, and in accord with Table 2. NO_2 performance improvements with the VIT simulation (red colours) occur across most
549 stations for the FAC2, MGE, RMSE, COA and IOA scores (Figure 9 (a,c,e,f,g)), while r and |MB| scores are more variable,
550 with some stations having better performance for the No VIT simulation. PM2.5 performance improvements are more mixed,
551 with large improvements for correlation coefficient (Figure S3(d)) and IOA (Figure S3(g), a mild but overall positive effect of
552 VIT for MGE, RMSE and COE (Figure S3(c,e,f)), and more stations showing a degradation of performance for FAC2 and
553 |MB|, echoing the net effect for these last two metrics seen in Table 2. O_3 performance shows a strong regional variation
554 (Figure S4): most scores improve with the use of the VIT parameterization in the western and north-eastern parts of the
555 continent, and degrade in the south-eastern USA. The degradation in the south-eastern (e.g. increases in O_3 concentrations in
556 a region which already experiences a positive O_3 bias) are associated with the transport of urban O_3 precursors into forested
557 areas in the region, with additional O_3 production occurring there. These effects may be removed through the introduction of
558 an additional parameterization for the reduced turbulence and shading within forested canopies (Makar *et al.*, 2017; Figure
559 S5), with the combined parameterizations resulting in improvements in both NO_2 and O_3 performance. While the use of VIT
560 degrades O_3 performance in this region, this degradation is thus very small relative to the large improvements noted with the
561 canopy effect (see Makar *et al.*, 2017; Figure S5 and its associated discussion in the S.I.). Another significant feature is the
562 improvement (red colours) in most O_3 station scores in urban regions (Figure S4). These improved scores largely result from
563 increases in ozone in the early morning hours (Figure 7(e)), where VIT has resulted in increased vertical mixing, reducing
564 surface level NO_x and hence NO_x titration of ozone, and also by mixing higher ozone levels aloft down into the lowest model
565 layer.

566 Overall, the impact of the VIT parameterization was to improve North American simulation accuracy, across multiple
567 statistical metrics, with the most significant improvements in the model performance for simulated NO_2. Spatially, model
568 performance was generally greatest in urban regions and western and northeastern North America, though this depends on the
569 chemical species and the performance metric chosen.

570 **3.7 Eastern North America 2.5km Grid Cell Size Domain Evaluation**

571 With the use of a smaller grid cell size (i.e. "higher resolution"), meteorological models and on-line air-quality models such
572 as GEM-MACH have the option of employing theoretical approaches which better simulate the more complex radiative
573 transfer and physical environment-induced turbulence of urban areas. Urban heat islands are known to have a significant effect
574 on turbulence, for example (Mason, 2000; Makar *et al.*, 2006). In these simulations, we make use of the Town Energy Balance

575 (TEB; Mason, 2000; Leroyer *et al.*, 2014; Lemonsu *et al.*, 2005), a single-layer urban canopy module which solves the

576 equations for urban atmosphere's surface and energy budgets for a variety of urban elements (roads, walls, roofs), then

577 aggregates the results for the net urban canopy. Such parameterizations are inappropriate for use in larger grid cell size models

578 due to the latter's inability to resolve individual surface types and spatial gradients at the city scale. An important consideration

579 in determining the relative importance of vehicle-induced turbulence is whether improvements in performance still occur,

580 when these other sources of turbulent kinetic energy are included explicitly. We address this issue in our 2.5km grid cell size

581 modelling by employing the TEB parameterization, for both VIT and No VIT simulations, evaluating both simulations against

582 surface monitoring network observations as before. Both summer and winter simulations were carried out on the blue domain

583 of Figure 5(b), and the same performance metrics were calculated as for the larger North American simulations (Table 3).

584 A similar pattern of performance improvement can be seen between 10km and 2.5km grid cell size domains, comparing Tables

585 2 and 3, with improvements due to the use of VIT predominating in both summer and winter: despite the addition of a more

586 explicit urban radiative balance approach, better scores were achieved with the addition of the VIT parameterization. Note that

587 comparisons between the 2.5km and 10km simulations for similar emissions inputs appear elsewhere in the literature (Stroud

588 *et al.*, 2020). The number of improved scores increases from summer to winter. Stable atmospheric conditions and low

589 meteorological turbulence levels are more common in winter than summer, during both day and night, and the impact of the

590 additional source of turbulence is thus proportionally stronger in the winter season. The VIT effects at the urban scale are the

591 strongest for NO_2 and PM2.5, and less noticeable for simulated O_3, similar to the North American domain simulation. The

592 largest improvements for the three species and across seasons occur for winter PM2.5, with the improved performance taking

593 place in the first or second digit of the given metric. Metric differences for NO_2 aside from mean bias occur in the second to

594 third digit in the winter, with summer differences occurring in the first to 2nd digit. Changes to O_3 are relatively minor, with

595 some improvements and degradation in performance in the 3rd digits across the different metrics.

596 UT-hour average differences between the two 2.5km grid-cell size simulations, for the three species evaluated for the summer

597 and winter simulations, appear in Figures (S6, S8), and Figures (10, 12) respectively. The summer differences in surface

598 concentration (Figure S6) are the largest at 6 AM local time (10UT; first column of panels), and have largely decreased to near

599 zero by 6 PM (22 UT; last column). Corresponding concentration vertical distribution differences along a cross-section linking

600 the major cities show the early morning depletion (increase) of NO_2, PM2.5 (O_3) are coupled to increases (decreases) aloft

601 (Figure S7, first column of panels). NO_2 and PM2.5 reductions extend to altitudes of up to 2km with the increase in radiative-

602 driven turbulence during the day, while the change in NOx/VOC regime aloft leads to increases in lower Troposphere O_3

603 (Figure S7, second column). Daytime mixing increases lead to a reduction in the effect by nightfall (Figure S7, third column).

604 VIT-enhanced transport of NO_2 from urban to rural areas can also be seen (Figure S6, center column/first column; note

605 increases in NO_2 on the periphery of the urban areas, pink to red colours). This additional NO_x added to NO_x-limited regions

606 leads to low-level (mostly sub-ppbv) increases in daytime O_3 at 10AM which persist through to 6PM. Over the Great Lakes,

607 the change in vertical transport on land, coupled with daytime lake breeze circulation (Makar *et al.*, 2010; Joe *et al.*, 2018;

608 Stroud *et al.*, 2020) results in a decrease in daytime NO_2 and PM2.5 over the Lakes and corresponding late-afternoon O_3

609   increases (Figure S6, blue colours in centre column of panels over the lakes for NO_2 and PM2.5, red colours in the final panel

610   of the sequence for O_3). The changes in the near-roadway environment thus have larger regional effects, changing the pathway

611   and reaction chemistry of transported chemicals on a regional scale.

612   The stronger impact of VIT under winter conditions is illustrated in Figures 10 and 11; NO_2 decreases (Figures 10, 11 (a,b,c))

613   persist throughout the day, though to a lower degree by 6 PM (contrast Figures S6,S7 (a,b,c) to Figures 10,11 (a,b,c)). The

614   vertical influence of VIT reaches an altitude of approximately 2 km in the winter (1 km in the summer); contrast Figure S7

615   and Figure 11. The absence of winter biogenic hydrocarbon production during the day has likely limited the daytime increase

616   in O_3 to the cities (compare Figure S6(h) with Figure 10(h)).   The large effect of VIT along major roadways can be seen in

617   both Figures S6 and Figure 10, particularly in the 6AM column of panels (a,d,g) in both figures, with the greatest reductions

618   aside from urban regions occurring along major roadways (e.g. Chicago to Detroit area).

619   The spatial extent of the region where the wintertime mean values for the PanAm domain differ at greater than 90% confidence

620   are shown in Figures 12 and 13 for the model's surface concentrations and the corresponding vertical cross-section,

621   respectively. The corresponding summertime differences for this domain are shown in Figures S8 and S9. For the wintertime

622   PanAm domain simulations, surface NO_2 and PM2.5 90% confidence regions are similar to those of the continental 10km

623   domain, and can be seen to extend into the late morning hours (14 UT; 10 AM local time; Figure 12(b,e)). The mean values

624   of NO_2 and to a lesser extent PM2.5 also differ at greater than 90% confidence later in the day in the urban core regions (Figure

625   12(c,f)). In contrast to the continental scale results (Figure 8) the influence of VIT on surface O_3 approaches but remains

626   below the 90% confidence level at 14 UT in the urban regions (Figure 12(h)), and remains below 90% confidence at the other

627   times shown. The vertical influence of wintertime VIT results in mean values differing at greater than 90% confidence up to

628   ~700m altitude for NO_2 and PM2.5, and the above-ground O_3 mean values differ at greater than 90% confidence for regions

629   between 25 and 200m altitude over specific large urban areas (e.g. New York City at 14 UT, Figure 13(h)). Regions of greater

630   than 90% confidence in the vertical at 22 UT for NO_2 and PM2.5 are confined to the urban core regions near the surface (Figure

631   13(c,f)). For the summertime high resolution PanAm domain simulations, differences at greater than 90% confidence occur

632   for surface NO_2 and PM2.5 at night and early morning (Figures S8,S9 (a,d)) and persist until later morning over parts of the

633   Great Lakes (Figure S8(b,e)), and isolated locations over cities (Figure S9(b,e)). Differences in the mean ozone aloft occur at

634   night at greater than 90% confidence occur over the largest cities (e.g. New York, Figure S9(a)).

635   Taken together, Figures 8, 12, 13, S8 and S9 show that the incorporation of VIT into the model results in mean values which

636   are statistically different at the 90% confidence level, for NO_2 and PM2.5 over large regions, and to a lesser degree for O_3 over

637   urban areas, with a greater influence at night, in the early morning, and under the more stable conditions of winter compared

638   to summer.

639   Differences in station-specific performance scores for the two simulations for the 2.5km grid-cell size domain, constructed as

640   for the 10km domain, are shown in Figures S10, S11, and S12 (summer) and Figures S13, S14 and S15 (winter) for NO_2,

641   PM2.5 and O_3, respectively.

642 The summer scores (Figs. S10, S11, S12) show the most significant improvements in the urban areas across all performance

643 metrics, with the largest relative magnitude differences for NO_2 and PM2.5, and lower magnitude changes for O_3. As for the

644 North American simulations, O_3 performance improvements occur in the cities, due to increased vertical mixing, and, O_3 scores

645 in rural regions have degraded, but may be improved with the use of a forest canopy parameterization, as discussed further in

646 the SI (Figure S5 and related text,, S12, and S15). The overall impact of the incorporation of the VIT parameterization is

647 clearly a positive one, particularly in urban areas: VIT has been shown to have a significant impact on summertime urban and

648 suburban scale photochemistry.

649 The metrics of the winter 2.5km station-specific evaluation for NO_2 (Figure S13) show both local improvements and

650 degradation in performance, depending on location. Wintertime PM2.5 performance improves substantially across most

651 metrics and most locations (Figure S14). Wintertime ozone performance is variable, though improvements can be seen for

652 most metrics within the largest urban areas (Figure S15).

653 **4 Discussion and Conclusions**

654 Our work implies that the turbulence associated with vehicle motion is capable of having a significant effect on the

655 concentrations of key pollutants in the lower atmosphere, using a parameterization which allows these effects to be

656 incorporated at the relatively coarse horizontal resolutions of regional chemical transport models. Incorporating that effect

657 into both continental-scale and higher resolution regional/urban scale air implementations of a pollution model resulted in an

658 overall improvement in model performance, across several different performance metrics. The improvement at higher

659 resolution (when the TEB urban parameterization was included in the model setup) implies that the mixing associated with

660 urban radiative transfer and roughness is not sufficient to account for the observed pollutant concentrations; the effect of VIT

661 is robust despite differences in radiative transfer schemes and across different horizontal resolutions.

662 However, we also acknowledge several limitations of our VIT formulation and have recommendations for future work which

663 would allow it to be improved and the uncertainties in our analysis reduced.

664 First, we have assumed that single-vehicle induced turbulence accounts for all of the turbulent kinetic energy contributed by

665 vehicles (Gordon *et al.*, 2012; Miller *et al.*, 2018). The passage of multiple vehicles also induces a "wake flow" in their

666 direction of motion. While this effect has been recognized in very high resolution roadway-scale models (Eskridge and

667 Catalano, 1987; Eskridge *et al.*, 1991), the breakdown of opposing wake flows into turbulence (arising from two-way traffic

668 and/or multiple lanes of traffic travelling at different speeds) has not been examined, to the best of our knowledge. However,

669 these wake flows are of sufficiently high energy that their residual power is being harnessed via vertical-turbine wind power

670 generation systems in both Turkey (Devecitech, 2020) and Scotland (Shell, 2020). The single-vehicle additive

671 parameterization we have created here may thus underestimate the net turbulent effect of vehicle passage. At the same time,

672 our assumption that individual VIT within a grid cell is simply additive may also be incorrect, resulting in overestimates of

673 that portion of the net VIT. With the advent of Doppler LIDAR systems with sufficient time resolution to capture turbulence,

674 we advocate for and are currently embarking on new observation studies employing these systems in scan mode across

675 highways, to fully characterize all vehicle-induced contributions to turbulence as a function of the number and type of vehicles

676 crossing below a LIDAR scan path perpendicular to the highway.

677 Second, our assumption that each vehicle's pathway crosses the grid cell is a considerable source of uncertainty. There we are

678 limited by the lack of availability of simultaneous vehicle speed and number data. However, recent developments in satellite-

679 based radar technology have been shown to provide accurate estimates of the speed of individual vehicles along major

680 highways (Meyer $et\ al.$, 2006; Bethke $et\ al.$, 2006), and binning and collection of these data may improve the linkage between

681 the more commonly available vehicle-km-travelled data and VIT beyond that used here. Other sources of gridded vehicle

682 and/or road density data (World Bank, 2018) should also be explored.

683 Third, one consideration for our parameterization is the issue of "traffic jams"; a large number of vehicles being present on the

684 road without much motion in such conditions. However, we note that in this case, the number of vehicles crossing a point in

685 space will drop – that is, if the underlying traffic data (vehicle-km-travelled) is of sufficient quality that traffic jams are

686 included, the existing parameterization should adequately handle these effects. Both our second and this third consideration

687 argue for the creation of more accurate vehicle travel data for use in air-quality models.

688 Last, we note that the ambient concentrations of pollutants such as NO_2, O_3 and PM2.5 are influenced by a host of factors

689 included in other parameterizations of air-quality models, and in the quality of the available emissions data. However, we

690 have shown here that improvements in the forecast quality of three different species with human-health impacts may be

691 achieved through the same process improvement. An examination of all of the other possible sources of error in air-quality

692 models is beyond the scope of this work. This work is not intended to be taken as a review or critique of existing boundary

693 layer parameterizations within meteorological or regional air-quality models. There has been excellent work in recent years

694 on improving these parameterizations, and there are several reviews discussing this topic in the literature (e.g. Edwards et al.,

695 2020). Rather, we focus here on an ancillary problem specific to regional air-quality models: whether the turbulent kinetic

696 energy associated with vehicle motion could account for sufficient sub-grid-scale vertical mixing to influence the

697 concentrations of fresh surface-emitted pollutants, at and above roadways, and further downwind. That is, on the extent to

698 which the at-source vertical transport of fresh pollutants from the mobile sector needs to take into account local sources of

699 energy for transport at the point of emission (whether in large stacks (Gordon $et\ al.$, 2018; Akingunola $et\ al.$, 2018) or over

700 roadways (as examined here)).

701 Despite the uncertainties identified above, our analysis has shown:

702 (1)   The drop-off of VIT with height above moving vehicles is well-represented by a Gaussian distribution, from multiple

703 measurement and computational fluid dynamics modelling studies.

704 (2)   The mixing lengths inferred from these studies ranges from 2.50 m (for individual isolated cars) through ~10 m

705 (vehicle ensembles) to 41 m (vehicle ensembles in a street canyon environment). We also note that the gradient in the net

706 thermal turbulent transfer coefficients drives concentration changes due to VIT. The expectation that VIT is capable of vertical

707 transport out of the lowest layers of a regional model is therefore a reasonable one.

708 (3) The magnitude of the localized energy input from VIT, while smaller than the input of solar energy during daylight
709 hours, is equivalent in magnitude to the energy perturbations resulting from the use of a state-of-the-art urban radiative balance
710 model (TEB; see Methods). That is, locally, VIT has sufficient energy to be equivalent to the impact of an improved urban
711 radiative transfer scheme – underlining its importance for vertical transport of pollutants.

712 (4) The impact of VIT depends on both local traffic conditions and the background meteorological conditions, with the
713 maximum effect occurring when turbulence in the ambient atmosphere is relatively weak (night through early morning), and
714 traffic levels are relatively high (morning rush hour).

715 (5) The use of the VIT parameterization has been demonstrated to result in decreases in air-quality model error, across
716 three different key pollutants, with the most striking results for mean biases, without resorting to the use of imposed minima
717 in the thermal turbulent exchange coefficients frequently used in air-quality models. These differences occur at greater than
718 90% confidence over much of the model domains for NO_2 and PM2.5, and in urban core regions for O_3 at 10km resolution, as
719 well as up to hundreds of metres above the surface.

720 (6) VIT has a significant impact on the rapid vertical distribution of freshly emitted pollutants on the very localized scale
721 of roadways where the enhanced mixing occurs, in analogy to the rapid vertical transport used in parameterizations of plume
722 rise from large stacks. Its impact on mixing of pre-existing meteorological and chemical variables on the grid-cell scale is
723 expected to be small.

724 Based on these findings, we conclude that VIT has a significant impact on pollutant transport and dispersion out of the lowest
725 layer of the atmosphere, and recommend its inclusion in regional air-quality models. Further improvements to the
726 parameterizations found herein would result from additional observations of TKE using Doppler lidar techniques, of vehicle
727 ensembles under realistic driving conditions.

728 **Acknowledgments**
729
730 The authors would like to acknowledge the contract assistance of Elisa Boutzis under the direction of J. Zhang in the generation
731 of VKT gridded fields.
732

733 **References**
734
735 Abelsohn, A., and Steib, D.M., Health effects of outdoor air pollution: approach to counseling patients
736   using the Air Quality Health Index, Can. Fam. Phys., 57, 881-887, 2011.
737 Adelman, Z., Baek, B.H. , Brandmeyer, J., Seppanen, C., Naess, B., and Yang, D., Spatial Surrogate
738   Development for 2014 Emissions Modeling Platforms, *2017 International Emissions Inventory*

739 *Conference,* Aug. 14-18, Baltimore, MD, USA, 2017 (see
740 https://www.epa.gov/sites/production/files/2017-11/documents/surrogate_developement.pdf).

741 AirNow, 2020: https://www.airnow.gov/, last accessed February 21, 2020.

742 Akingunola, A., Makar, P.A., Zhang, J., Darlington, A., Li, S.-M., Gordon, M., Moran, M.D., Zheng, Q.,
743 A chemical transport model study of plume-rise and particle size distribution for the Athabasca oil
744 sands, Atmos. Chem. Phys., 18, 8667-8688, 2018.

745 Bou-Zeid, E., Meneveau, C., Parlange, M.B., Large-eddy simulation of neutral atmospheric boundary
746 layer flow over heterogeneous surfaces: Blending height and effective surface roughness, Water
747 Resources Research, 40, W02505, doi:10.1029/2003WR02475, 2004.

748 Bethke, K.-H., Baumgartner, S., Gabele, M., Hounam, D., Kemptner, E., Klement, E., Krieger, G., and
749 Erxleben, R., Air- and spaceborne monitoring of road traffic using SAR moving target indication –
750 Project TRAMRAD, ISPRS J. Phot. Remote Sens., 61, 243-259, 2006.

751 Bradshaw, P., Possible origin of Prandt's mixing-length theory, Nature, 249, 135–136.
752 Bibcode:1974Natur.249..135B. doi:10.1038/249135b0, 1974.

753 Briggs, G.A.: Plume rise predictions, Lectures on air Pollution and environmental impact analyses. In:
754 Workshop Proceedings, Sept. 29-Oct. 3, pp. 59-111, *American Meteorological Society*, Boston, MA,
755 USA., 1975.

756 Briggs, G.A.: Plume rise and buoyancy effects, atmospheric sciences and power production. In:
757 Randerson, D. (Ed.), DOE/TIC-27601 (DE84005177), TN. Technical Information Center, U.S. Dept.
758 of Energy, Oak Ridge, USA,.pp 327-366, 1984.

759 Caron, J-F., Milewski, T., Buehner, M., Fillion, L., Reszka, M., Macpherson, S., St-James, J.,
760 Implementation of deterministic weather forecasting systems based on ensemble-variational data
761 assimilation at Environment Canada. Part II: The regional system. Mon. Wea. Rev. 143: 2560– 2580,
762 doi:10.1175/MWR-D-14-00353.1, 2015.

763 Chen, J. and GEM-MACH development team, GEM-MACH atmospheric chemistry module for the GEM
764 numerical weather pre-diction model, Environment and Climate Change Canada, Zenodo,
765 https://doi.org/10.5281/zenodo.2579386, 2019, last accessed March 3, 2020.

766 Cote, J.C., Gravel, S., Methot, A., Patoine, A., Roch, M., Staniforth, A., The operational CMC-MRB
767 Global Environmental Multiscale (GEM) Model. Part I: design considerations and formulation, Mon.
768 Wea. Rev., 126, 1373-1395, 1998(a).

769 Cote, J.C., Desmarais, J.-G., Gravel, G., Methot, A., Patoine, A., The operational CMC- MRB Global
770 Environmental Multiscale (GEM) Model. Part II: results. Mon. Wea. Rev., 126, 1397-1418, 1998(b).

771 Devecitech, 2020: https://devecitech.com/?page_id=5, last accessed February 21, 2020.

772 Di Sabatino S., Kastner-Klein, P., Berkowicz, R., Britter, R.E., and Fedorovich, E., The modeling of

773 turbulence from traffic in urban dispersion models – Part I: Theoretical considerations. Environmental

774 Fluid Mechanics, 3, 129-143, 2003.

775 EPA, 2017: Data available from US EPA:

776 ftp://newftp.epa.gov/air/emismod/2011/v3platform/2017emissions/2017ek_cb6v2_v6_11g_inputs_onro

777 ad.zip, last accessed March 3, 2020.

778 Eskridge, R.E., and Catalano, J.A., ROADWAY – a numerical model for predicting air pollutants near

779 highways, Users Guide, US EPA, 134pp, 1987 (also available at

780 https://nepis.epa.gov/Exe/ZyPDF.cgi/20015RHA.PDF?Dockey=20015RHA.PDF, last accessed

781 February 25, 2020).

782 Eskridge, R.E., Petersen, W.B., and Rao, S.T., Turbulent diffusion behind vehicles: effect of traffic speed

783 on pollutant concentrations, J. Air & Waste Management Ass., 41:3, 312-317, 1991. DOI:

784 10.1080/10473289.1991.10466848

785 Galmarini, S., Hogrefe, C., Brunner, D., Makar, P.A., Baklanov, A., Preface, Atm. Env., 115, 340-344,

786 2015.

787 Gordon, M., Makar, P.A., Staebler, R.M., Zhang, J., Akingunola, A., Gong, W., and Li, S.-M., A

788 comparison of plume rise algorithms to stack plume measurements in the Athabasca Oil Sands,

789 Atmos. Chem. Phys., 18, 14695-14714, 2018.

790 Gordon, M., Staebler, R.M., Liggio, J., Makar, P.A., Li, S.-M., Wentzell, J., Lu, G., Lee, P., and Brook,

791 J.R., Measurements of enhanced turbulent mixing near highways, J. App. Met & Clim., 51, 1618-

792 1632, 2012.

793 Hu, X.-M., Klein, P.M., and Xue, M., Evaluation of the updated YSU Planetary Boundary Layer Scheme

794 within WRF for Wind Resource and Air Quality Assessments. J. Geophys. Res. Atmos., 118, 10,490–

795 10,505, doi:10.1002/jgrd.50823, 2013.

796 Joe, P., Belair, S., Ber Nier, N.B., Bouchet, V., Brook, J.R., Brunet, D., Burrows, W., Charland, J.-P.,

797 Dehghan, A., Driedger, N., Duhamie, C., Evans, G., Filion, A.-B., Frenette, R., DeGrandpre, J.,

798 Gultepe, I., Henderson, D., Herdt, A., Hilker, N., Huang, L., Hung, E., Isaac, G., Jeong, C.-H.,

799 Johnston, D., Klassen, J., Leroyer, S., Lin, H., MacDonald, M., MacPhee, J., Mariani, Z., Munoz, T.,

800 Ried, J., Robichaud, A., Rochon, Y., Shairsing, K., Sills, D., Spacek, L., Stroud, C., Su, Y., Taylor,

801 N., Vanos, J., Voogt, J., Wang, J.M., Wiechers, T., Wren, S., Yang, H., Yip, T., The Environment

802 Canada Pan and ParaPan American science showcase project, Bull. Am. Met. Soc., 921-953, 2018.

803 Kain, J.S., The Kain-Fritsch convective parameterization: an update, J. App. Met., 43, 170-181, 2004.

804 Kastner-Klein P., Fedorovich, E., Ketzel, M., Berkowicz, R., and Britter, R., The modelling of turbulence
805   from traffic in urban dispersion models – Part II: Evaluation against laboratory and fullscale
806   concentration measurements in street canyons. Environmental Fluid Mechanics, 3, 145-172, 2003.

807 Kim, Y., Huang, L., Gong, S., Jia, C.Q., A new approach to quantifying vehicle induced turbulence for
808   complex traffic scenarios, C. J. Chem. Eng., 24, 71-78, 2016a.

809 Kim, S.-W., Barth, M.C., and Trainer, M., Impact of turbulent mixing on isoprene chemistry, Geophys.
810   Res. Lett., 43, 7701-7708, 2016.

811 Kim, Y., Sartelet, K., Raut, J-C., Chazette, P., Influence of an urban canopy model and PBL schemes on
812   vertical mixing for air quality modeling over Greater Paris, Atm. Env., 107, 289-306, 2015.

813 Kim, Y., Quantification of vehicle-induced turbulence on roadways using computational fluid dynamics
814   simulation, M.Sc. Thesis, Department of Chemical Engineering and Applied Chemistry, University
815   of Toronto, 93 pp., 2011.

816 Klein, P.M., Hu, X.-M., and Xue, M., Impacts of mixing processes in the nocturnal atmospheric
817   boundary layer on urban ozone concentrations. Boundary Layer Meteorology, 150, 107-130, 2014.

818 Lemonsu, A., Belair, S., Mailhot, J., Leroyer, S., Evaluation of the Town Energy Balance model in cold
819   and snowy conditions during the Montreal urban snow experiment, 2005, J. App. Met. Clim., 49, 346-
820   362, 2010.

821 Leroyer, S., Belair, S., Husain, S.Z., and Mailhot, J., Subkilometer numerical weather prediction in an
822   urban coastal area: a case study over the Vancouver metropolitan area, J. App. Met. Clim., 53, 1433-
823   1453, 2014.

824 Li, Y., Barth, M.C., Chen, G., Patton, E.G., Kim, S.-W., Wisthaler, A., Mikoviny, T., Fried, A., Clark,
825   R., and Steiner, A.L., Large-eddy simulation of biogenic VOC chemistry during the DISCOVER-AQ
826   2011 campaign, J. Geophys. Res. Atm., 121, 8083 – 8105, 2016.

827 Makar, P.A., Staebler, R.M., Akingunola, A., Zhang, J., McLinden, C., Kharol, S.K., Pabla, B., Cheung,
828   P. and Zheng, Q., The effects of forest canopy shading and turbulence on boundary layer ozone,
829   Nature Communications, 8, art. no. 15243, doi: 10.1038/ncomms15243, 2017.

830 Makar, P.A., Gong, W., Milbrandt, J., Hogrefe, C., Zhang, Y., Curci, G., Zabkar, R., Im, U., Balzarini,
831   A., Baro, R., Bianconi, R., Cheung, P., Forkel, R., Gravel, S., Hirtl, H., Honzak, L., Hou, A., Jimenz-
832   Guerrero, P., Langer, M., Moran, M.D., Pabla, B., Perez, J.L., Pirovano, G., San Jose, R., Tuccella, P.,
833   Werhahn, J., Zhang, J., Galmarini, S., Feedbacks between air pollution and weather, part 1: Effects
834   on weather. Atm. Env., 115, 442-469, 2015a.

835 Makar, P.A., Gong, W., Hogrefe, C., Zhang, Y., Curci, G., Zabkar, R., Milbrandt, J., Im, U., Balzarini,
836   A., Baro, R., Bianconi, R., Cheung, P., Forkel, R., Gravel, S., Hirtl, H., Honzak, L., Hou, A., Jimenz-
837   Guerrero, P., Langer, M., Moran, M.D., Pabla, B., Perez, J.L., Pirovano, G., San Jose, R., Tuccella, P.,

838   Werhahn, J., Zhang, J., Galmarini, S., Feedbacks between air pollution and weather, part 2: Effects
839   on chemistry. Atm. Env., 115, 499-526, 2015b.

840   Makar, P.A., Nissen, R., Teakles, A., Zhang, J., Zheng, Q., Moran, M.D., Yau, H., diCenzo, C., Turbulent
841   transport, emissions and the role of compensating errors in chemical transport models, Geo. Mod.
842   Dev., 7, 1001-1024, 2014.

843   Makar, P.A., Zhang, J., Gong, W., Stroud, C., Sills, D., Hayden, K.L., Brook, J., Levy, I., Mihele, C.,
844   Moran, M.D., Tarasick, D.W., He, H., and Plummer, D., Mass tracking for chemical analysis: the
845   causes of ozone formation in southern Ontario during BAQS-Met 2007, Atmos. Chem. Phys., 10,
846   11151-11173, 2010.

847   Makar, P.A., *et al.*, Anthropogenic heat flux, urban properties, and regional weather, Atm. Env. 40, 2750-
848   2766, 2006.

849   Mason, V., A physically-based scheme for the urban energy balance in atmospheric models, Bound. Lay.
850   Met., 94, 357-397, 2000.

851   Mensink, C., Lefebre, F., Janssen, L., and Cornelis, J., A comparison of three street canyon models with
852   measurements at an urban station in Antwerp, Belgium, Env. Mod. Soft., 21, 514-516, 2014.

853   Meyer, F., Hinz, S., Laika, A., Weihing, D., Bamler, R., Performance analysis of the TerraSAR-X Traffic
854   monitoring concept, ISPRS J. Phot. Remote Sens., 61, 225-242, 2006.

855   Milbrandt, J.A., Bélair, S., Faucher, M., Vallée, M., Carrera, M.L., and Glazer, A., The pan-Canadian
856   High Resolution (2.5 km) Deterministic Prediction System, Weather and Forecasting, 31 (6), pp.
857   1791-1816, 2016.

858   Miller, S.J., Gordon, M., Staebler, R.M., and Taylor, P.A., A study of the spatial variation of vehicle-
859   induced turbulence on highways using measurements from a mobile platform, Bound. Lay. Met.,
860   https://doi.org/10.1007/s10546-018-0416-9, 29 pp., 2018.

861   Moran, M.D., Lupu, A., Zhang, J., Savic-Jovcic, V., Gravel, S., A comprehensive performance evaluation
862   of the next generation of the Canadian operational regional air quality deterministic prediction system,
863   Springer Proceedings in Complexity, pp 75-81, 2018.

864   Moran M.D., S. Ménard, D. Talbot, P. Huang, P.A. Makar, W. Gong, H. Landry, S. Gravel, S. Gong, L-
865   P. Crevier, A. Kallaur, M. Sassi, Particulate-matter forecasting with GEM-MACH15, a new Canadian
866   air-quality forecast model. In: Steyn DG, Rao ST (eds) Air Pollution Modelling and Its Application
867   XX, Springer, Dordrecht, 289-292, 2010.

868   Ouwersloot, H.G., Vila-Guerau de Arellano, J., van Heerwaarden, C.C., Ganzeveld, L.N., Krol, M.C.,
869   and Lelieveld, J., On the segregation of chemical species in a clear boundary layer over heterogeneous
870   land surfaces, Atmos. Chem. Phys., 11, 10681-10704, 2011.

871   Prandtl, L., Z. angew, Math. Mech. 5 (1): 136–139, 1925.

872 Rao, K.S., Gunter, R.L., White, J.R., and Hosker, R.P., Turbulence and dispersion modeling near
873   highways, Atm. Env., 36, 4337-4346, 2002.

874 Rao, S.T., Sedefian, L., and Czapksi, U.H., Characteristics of turbulence and dispersion of pollutants near
875   major highways, J. App. Met., 18, 286-293, 1979.

876 Ren, S., Stroud, C., Belair, S., Leroyer, S., Moran, M., Zhang, J., Akingunola, A., and Makar, P., Impact
877   of Urban Land Use and Anthropogenic Heat on Air Quality in Urban Environments, Springer
878   Proceedings in Complexity, pp. 153-158, 2020.

879 Shell, 2020: https://www.shell.com/inside-energy/turbine-turns-traffic-into-energy.html, last accessed
880   February 21, 2020.

881 Stieb, D.M., Burnett, R.T., Smith-Doiron, M., Brion, O., Hwashin, H.S., and Economou, V., A new
882   multipollutant, no-threshold air quality health index based on short-term associations observed in
883   daily time-series analyses, J. Air W. Man. Ass., 58, 435-450, 2008.

884 Stroud, C., Ren, S., Zhang, J., Moran, M., Akingunola, A., Makar, P.A., Munoz-Alpizar, R., Leroyer, S.,
885   Bélair, S., Sills, D., Brook, J.R., Chemical analysis of surface-level ozone exceedances during the
886   2015 pan American games, Atmosphere, 11 (6), art. no. 572, 2020.

887 Taylor, B., National Pollution Release Inventory, Environment and Climate Change Canada, personal
888   communication, 2019.

889 Woodward, H., Stettler, M., Pavlidis, D., Aristodemou, E., ApSimon, H., and Pain, C.., A large eddy
890   simulation of the dispersion of traffic emissions by moving vehicles at an intersection, Atmospheric
891   Environment, 215, 116891, 2019.

892 World Bank, 2018: https://datacatalog.worldbank.org/dataset/grip-global-roads-inventory-dataset-2018-
893   road-density, last accessed February 21, 2020.

894 Vinuesa, J.-F., and Vila-Guerau de Arellano, J., Introducing effective reaction rates to account for
895   inefficient mixing of the convective boundary layer, Atmos. Environ., 39, 445-461, 2005.

896 Zhang, Y., Gu, Z., and Yu, C.W., Large eddy simulation of vehicle induced turbulence in an urban street
897   canyon with a new dynamically vehicle-tracking scheme, Aerosol and Air Quality Research, 17, 865-
898   874, doi: 10.4209/aaqr.2016.05.0204, 2017.

899

900

901
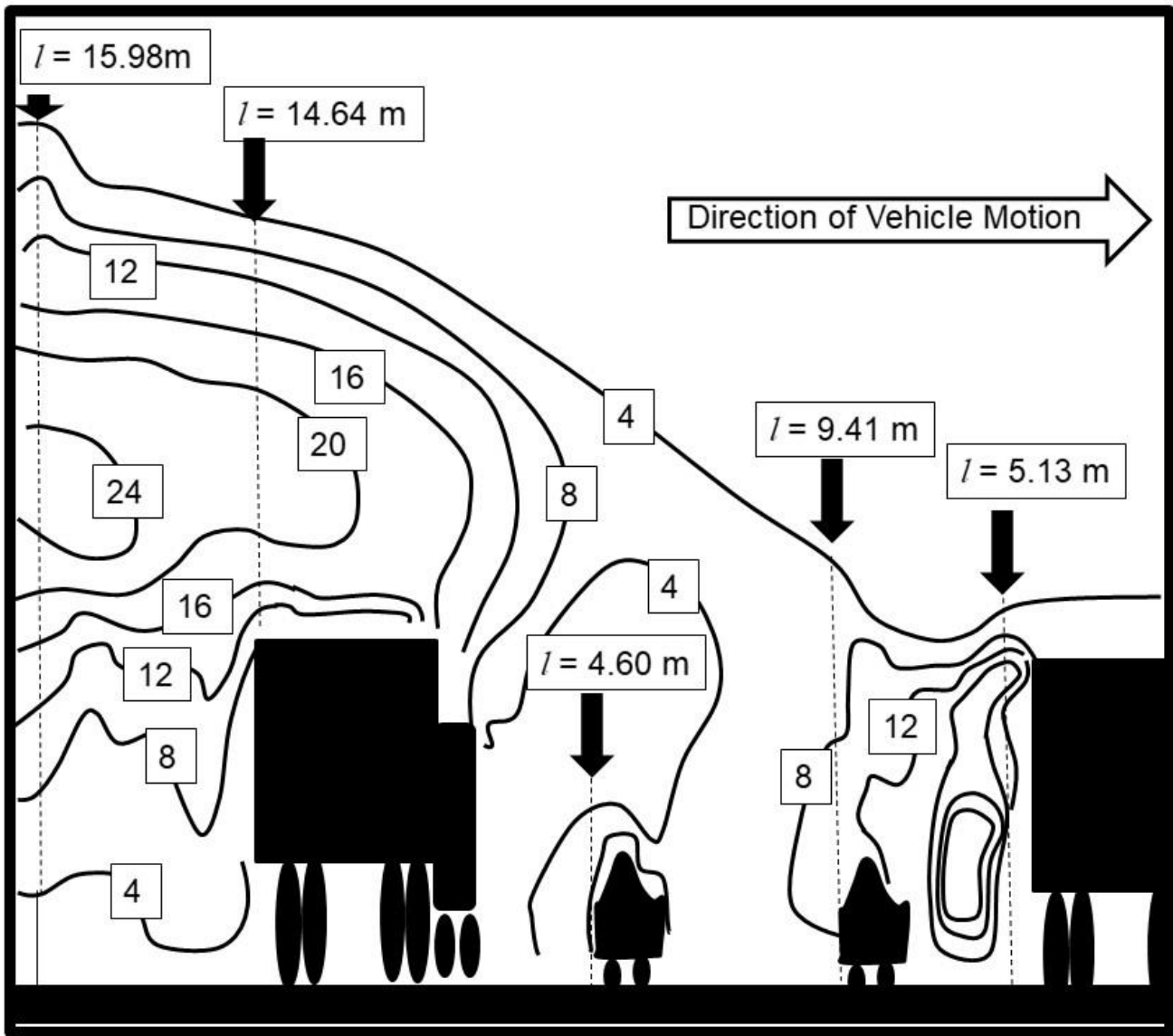
902

903 **Figure 1.** Example of length scales associated with an ensemble of vehicles (after Kim *et al.*, 2016, Figure 14). TKE contours along dashed
904 lines were extracted and fit to equations (1,2) for Table 1. Note that the length scale of turbulence immediately behind the leading vehicle,
905 a large transport truck is only 5.13 m, while the length scale immediately behind the trailing vehicle in the ensemble (an identical transport
906 truck) is 14.73 m.

907
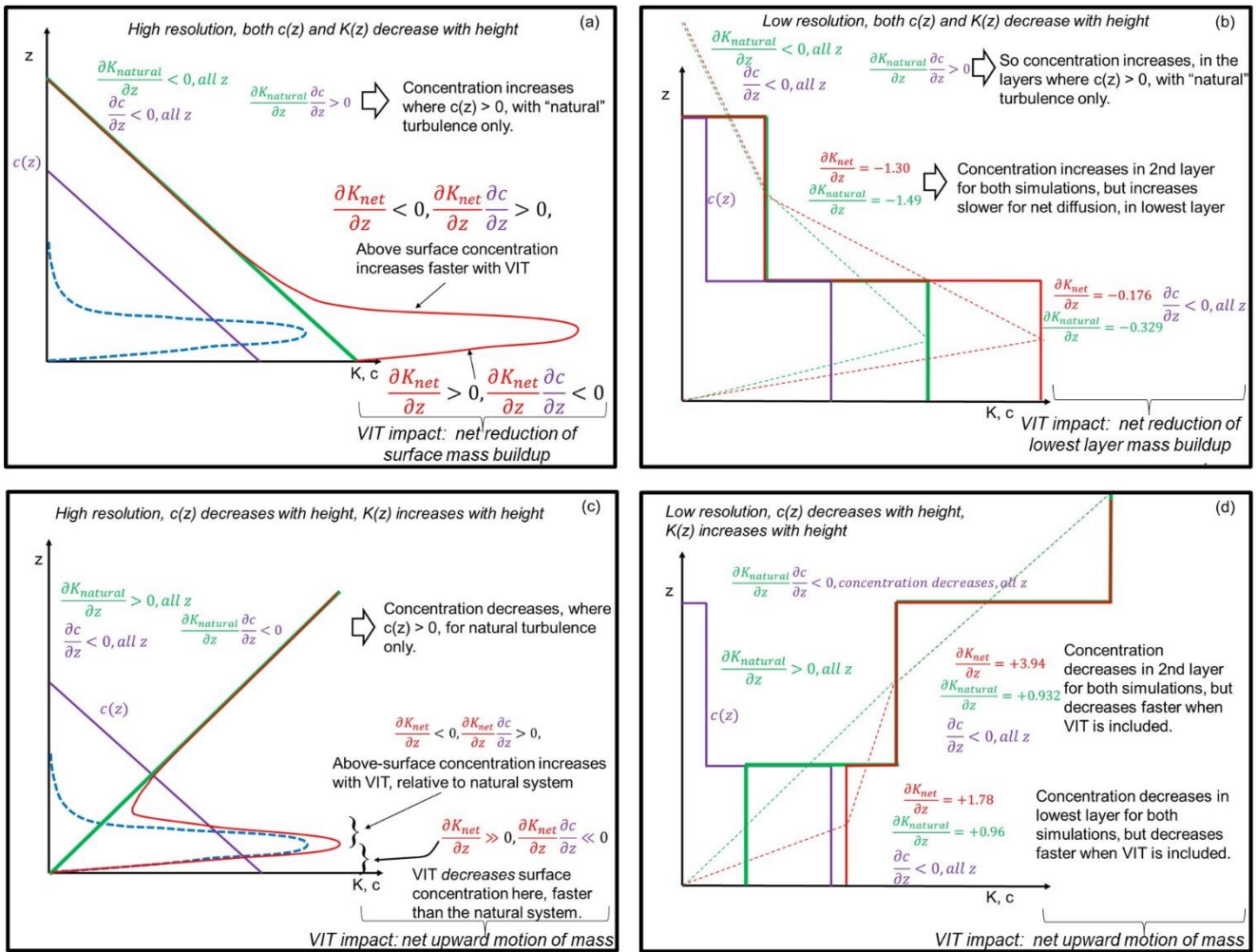
908

909 **Figure 2.** Illustration of the impact of VIT on the local vertical gradient of the thermal turbulent transfer coefficients, at high (a,c) and low
910 (b,d) resolution. Purple, green, dashed blue, and red lines illustrate the height variation of concentration, meteorological or natural coefficient
911 of thermal turbulent transfer, VIT coefficient of thermal turbulent transfer, and net coefficient of thermal turbulent transfer, respectively.
912 (a,b) High and low resolution profiles and gradients, for the case where both concentration and meteorological thermal turbulent transfer
913 coefficients decrease with height. (c,d) High and low resolution profiles and gradients, for the case where concentration decreases and
914 meteorological thermal turbulent transfer coefficients increases with height.

915
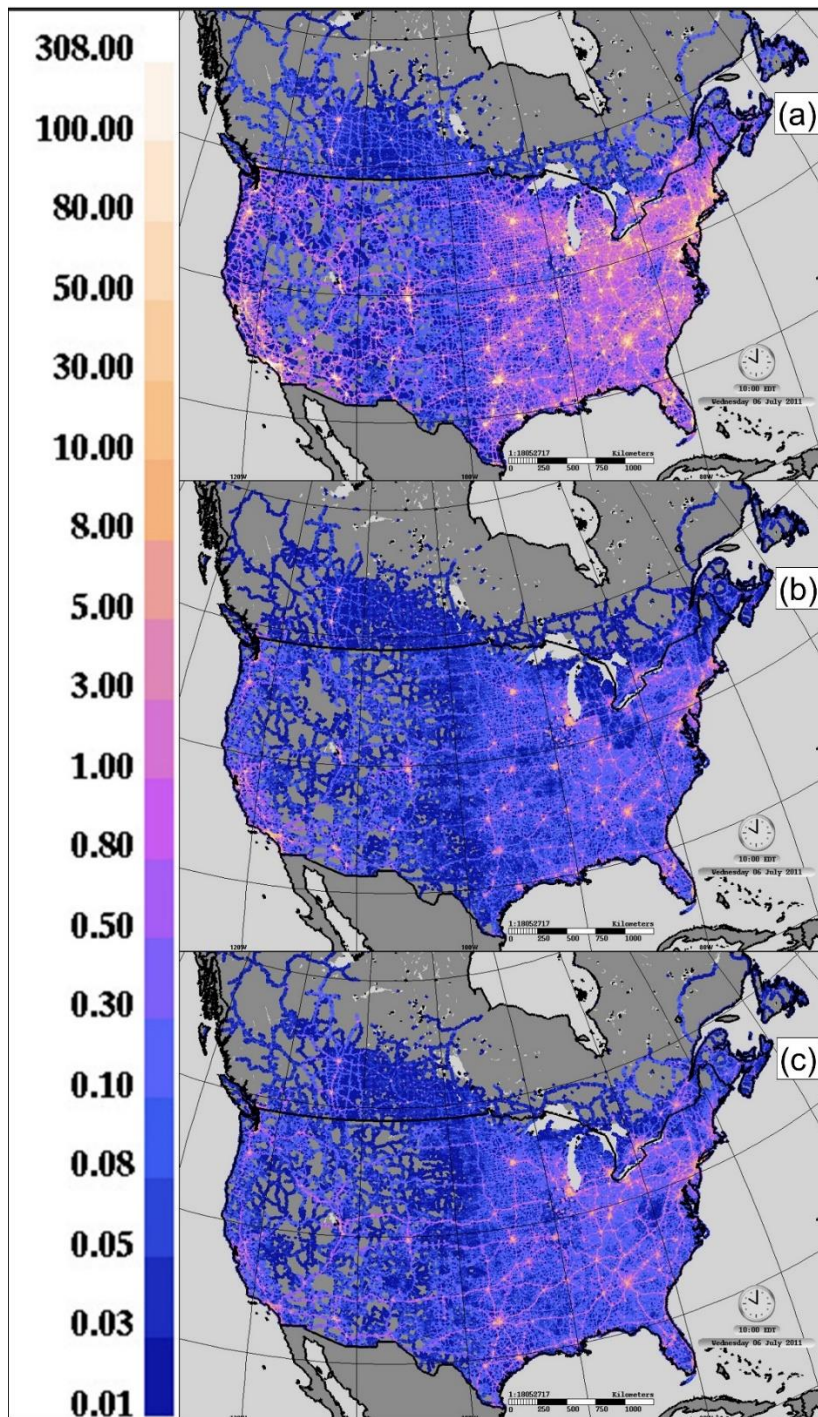
Figure 3. Vehicle km travelled per 10 km grid cell (km s^{-1}) for (a) cars, (b) mid-size vehicles and (c) trucks, July, 2015.

917

918
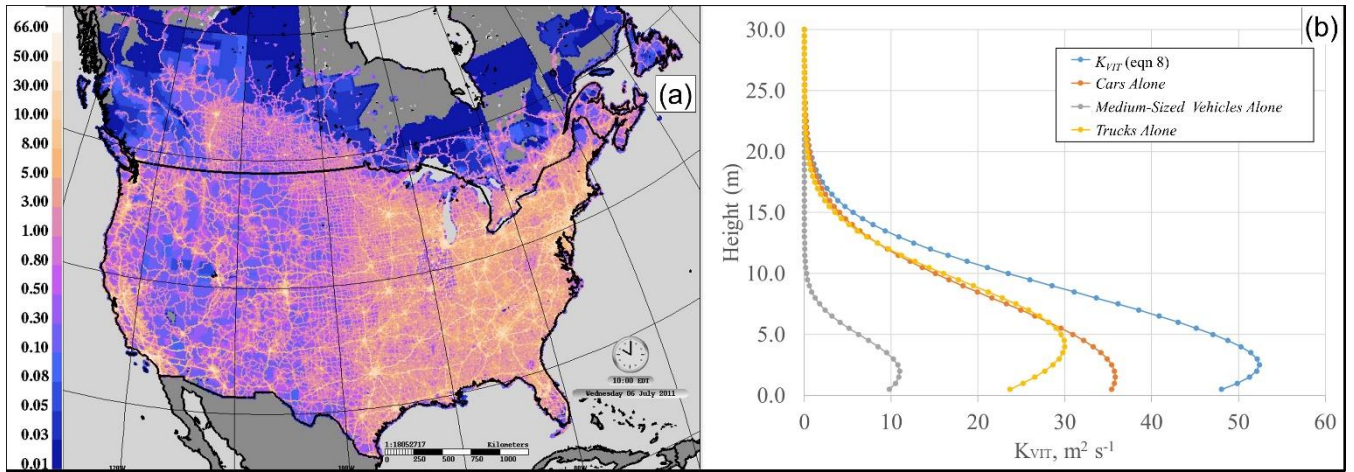
919
920 **Figure 4.** (a) Example estimated thermal turbulent transfer coefficients from VIT at 2 m elevation during a weekday at 10 am in July (m^{2}s$^-$
921 ^{1}), using the VKT data of Figure 3. (b) Vertical profile of VIT thermal turbulent transfer coefficients at one meter resolution in central
922 Manhattan Island, and individual values for the TKE associated with cars, mid-sized vehicles and trucks considered separately, generated
923 using equation (8). Note that the profiles of (b) would be added to the ambient thermal diffusivity coefficients (see section 2.5, and
924 equation (12)).

925
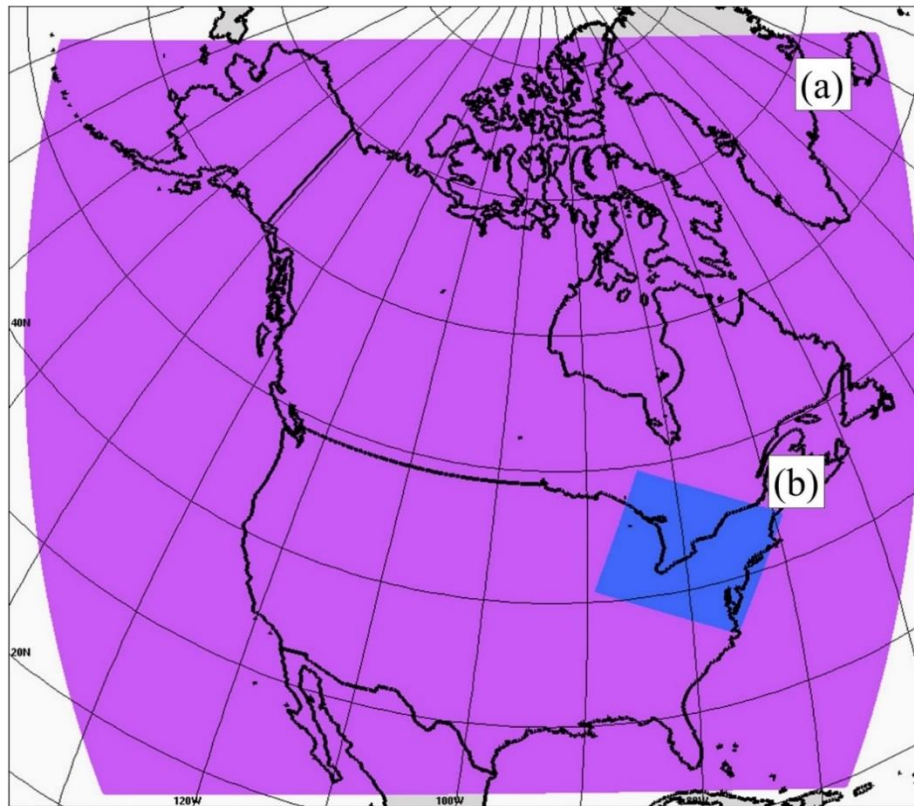
926

927   **Figure 5.** GEM-MACH test domains: (a) 10km grid cell size North American domain. (b) 2.5km grid cell size Pan Am domain.

928
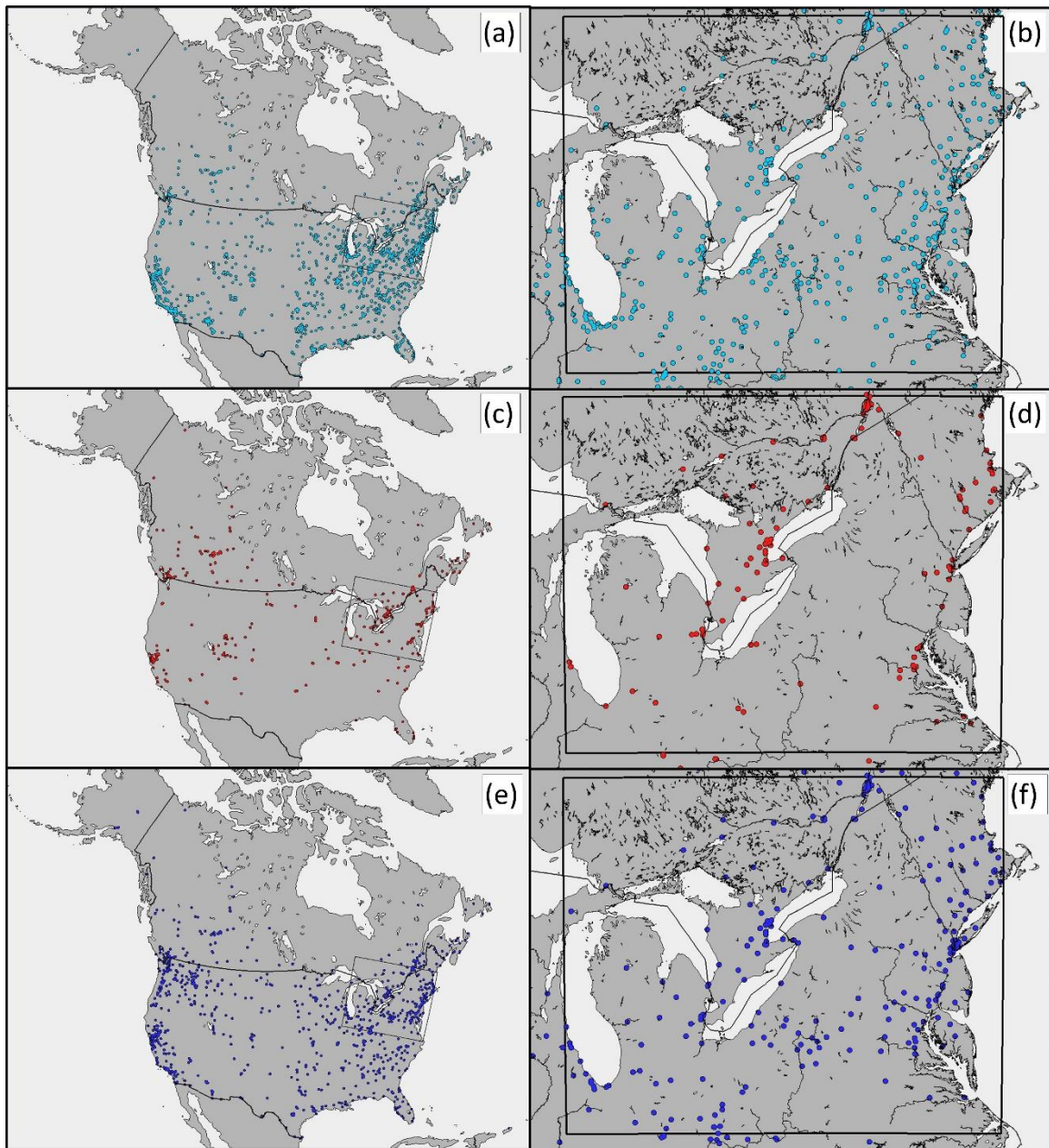
929
930 **Figure 6**. AIRNOW hourly observation station locations for ozone (a,b), nitrogen dioxide (c,d), and particulate matter with diameters less
931 than 2.5 μm (e,f). (a,c,e): Stations used for the 10km grid cell size domain evaluation. (b,d,f): Stations used for the 2.5km grid cell size
932 domain evaluation (all stations located within central box).

933
934
935
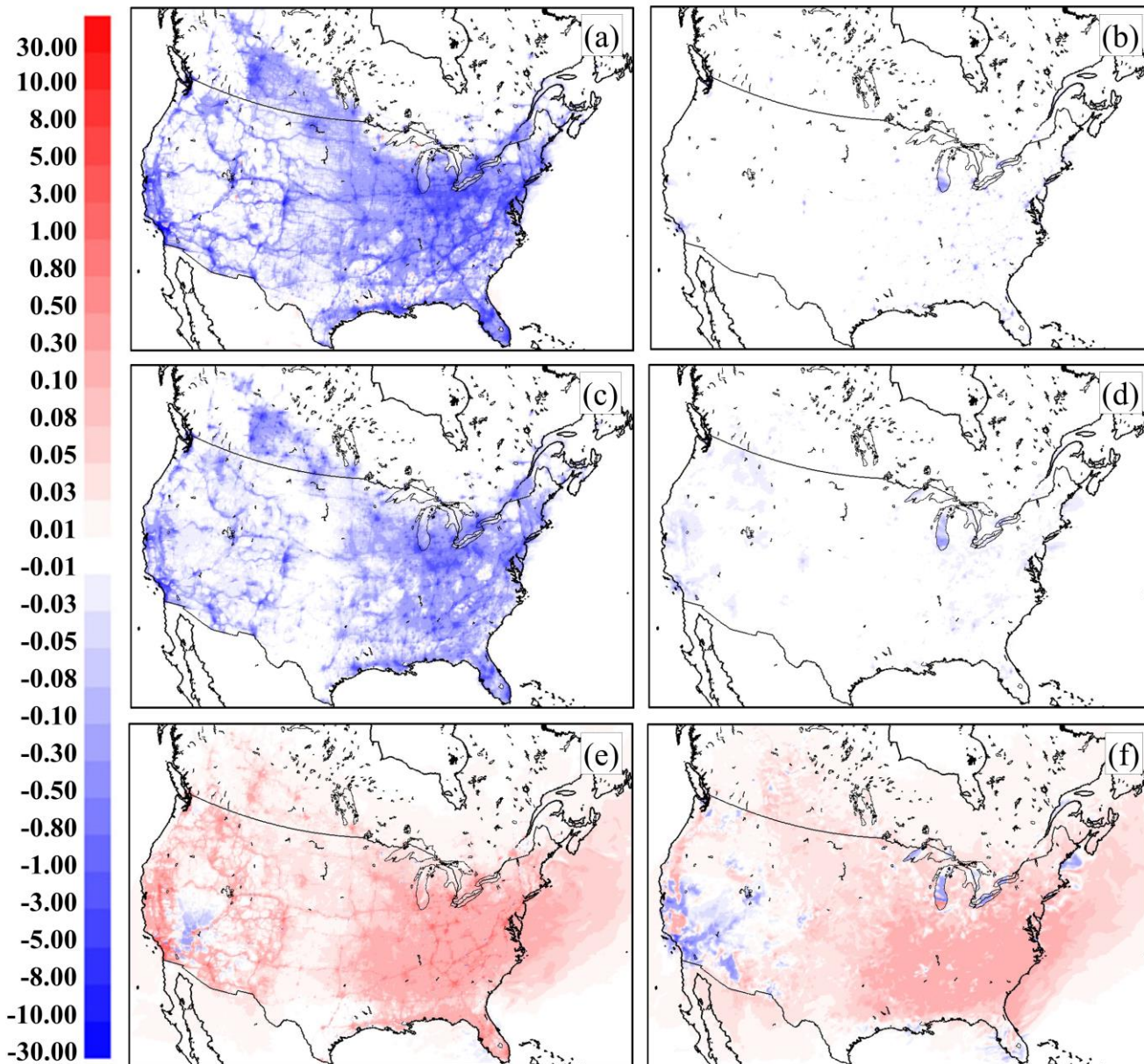
Figure 7. Difference in 29 day average NO$_2$, PM2.5 and O$_3$, July 2016 Continental 10km domain simulations (VIT simulation – No VIT simulation). Averages are paired at (a,c,e: 10UT, b,d,f: 22UT) according to species; (a,b): ΔNO$_2$(ppbv); (c,d) ΔPM2.5(μg m^{-3}); (e,f) ΔO$_3$(ppbv).
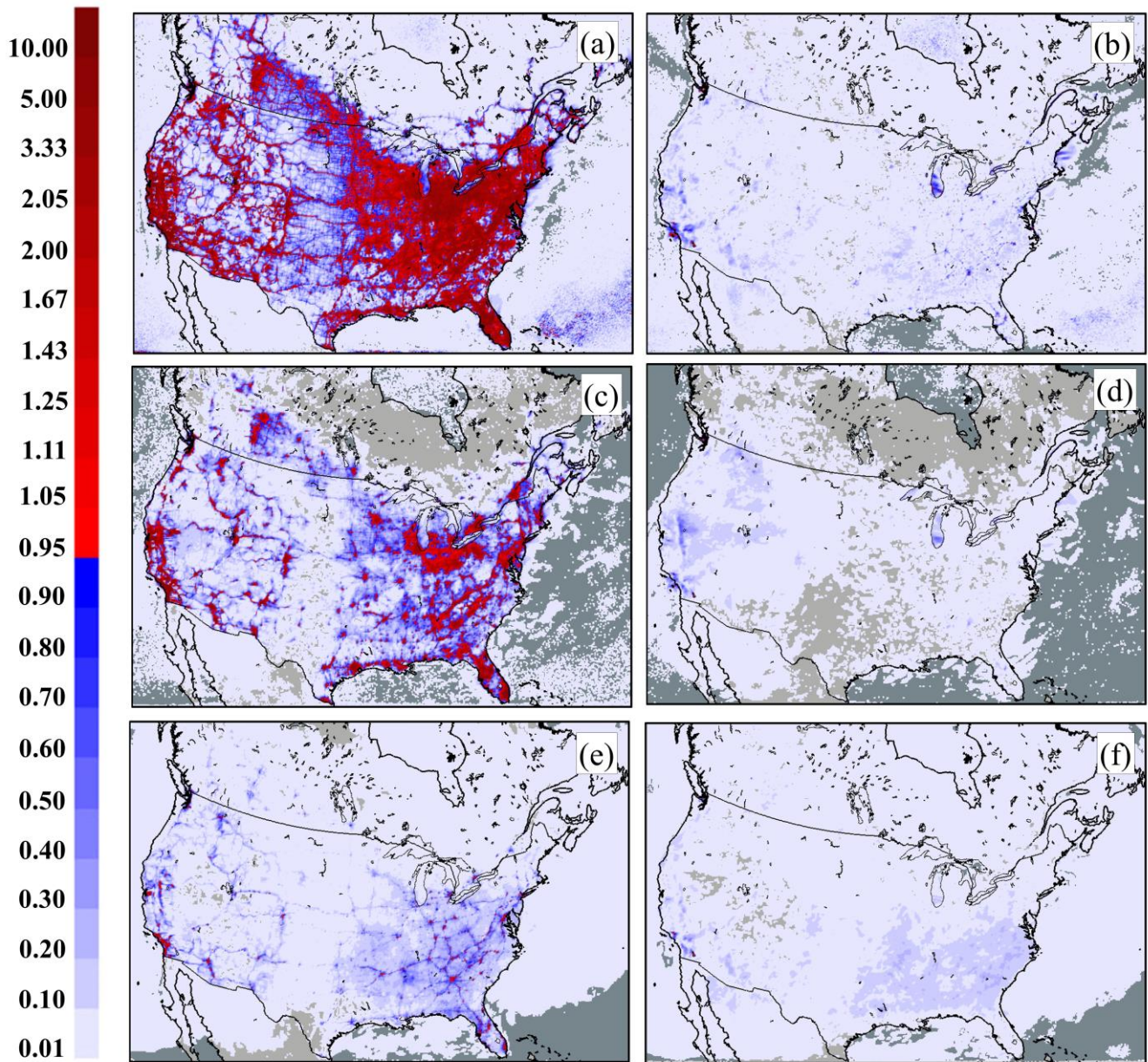
Figure 8. 90% confidence levels for the 29 day NO2, PM2.5 and O3 July 2016 Continental 10km domain simulations. Panels arranges as in Figure 7: (a,c,e): 10UT, (b,d,f): 22UT;,(a,b): NO$_2$, (c,d) PM2.5; (e,f) O$_3$. Values > 1.0 indicate that the simulations differ at greater than 90% confidence.

947
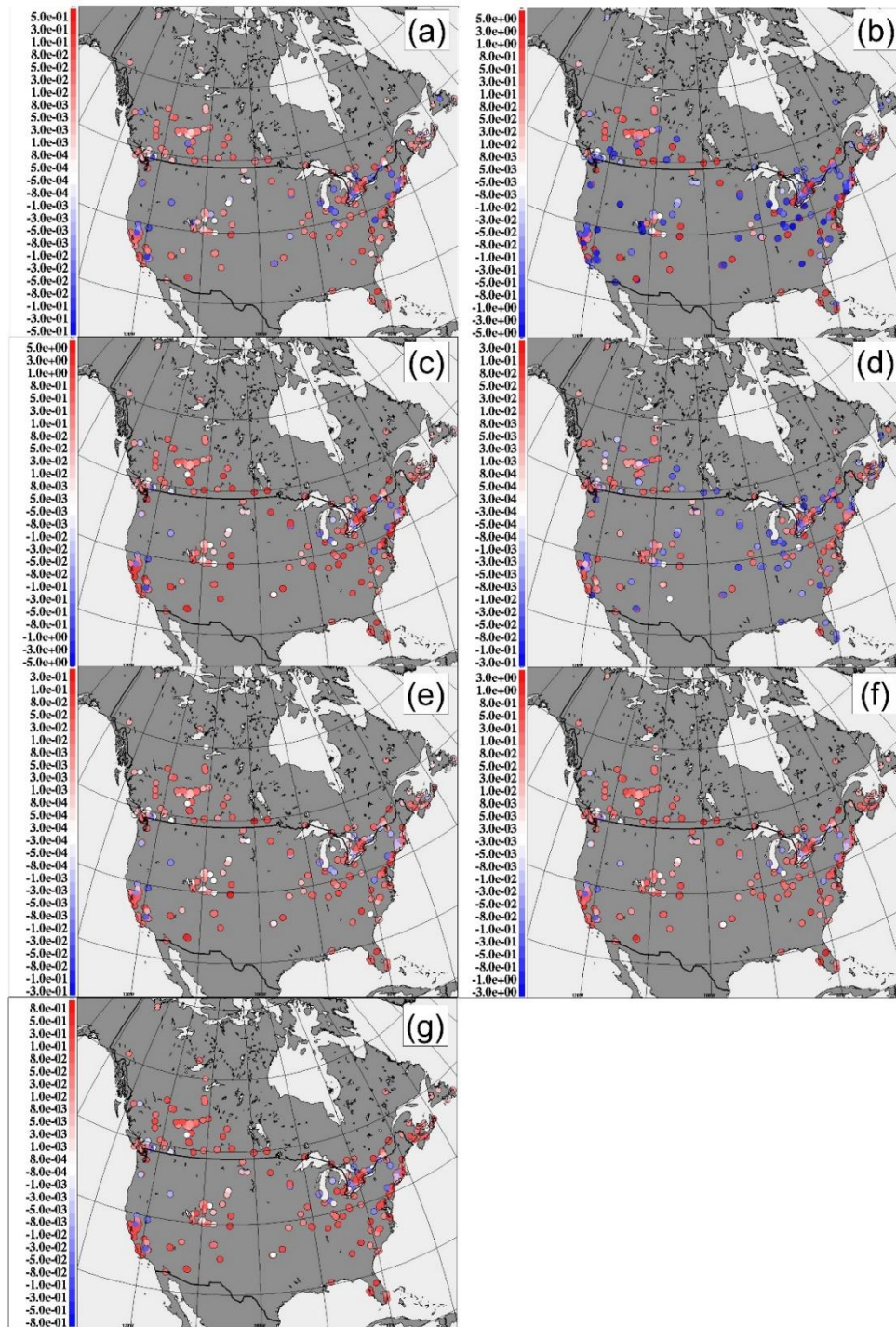
Figure 9. Change in model NO$_2$ performance at 358 North American surface monitoring sites, July 2016 (ppbv). Red colours indicate stations where the addition of the VIT parameterization improved model performance, blue colours indicate stations where the addition of the VIT parameterization degraded model performance. (a) $\Delta FAC2_{VIT-No\,VIT}$; (b) $\Delta|MB|_{No\,VIT-VIT}$; (c) $\Delta MGE_{No\,VIT-VIT}$; (d) $\Delta r_{VIT-No\,VIT}$; (e) $\Delta RMSE_{No\,VIT-VIT}$; (f) $\Delta COE_{VIT-No\,VIT}$; (g) $\Delta IOA_{VIT-No\,VIT}$.

952

953
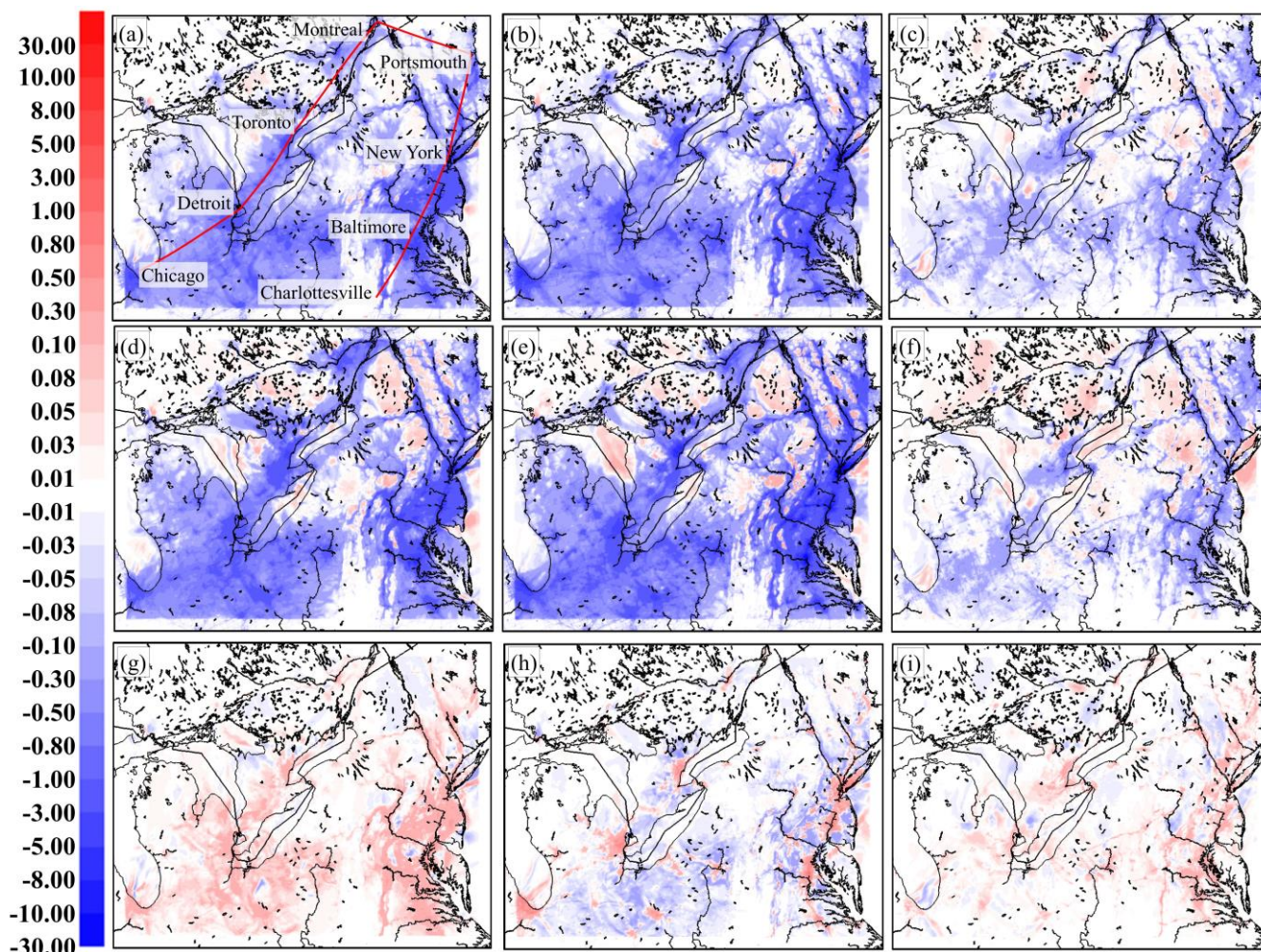
Figure 10. Difference in 30 day average surface NO₂, PM2.5 and O₃, January 2016, PanAm 2.5km grid cell size domain simulation. Averages are paired at (10, 14, and 22UT) according to species; (a,b,c): ΔNO₂;(ppbv) (d,e,f) ΔPM2.5 (μg m⁻³); (g,h,i) ΔO₃ (ppbv). Red line in panel (a) indicates position of vertical cross-section shown in Figure 11.

958
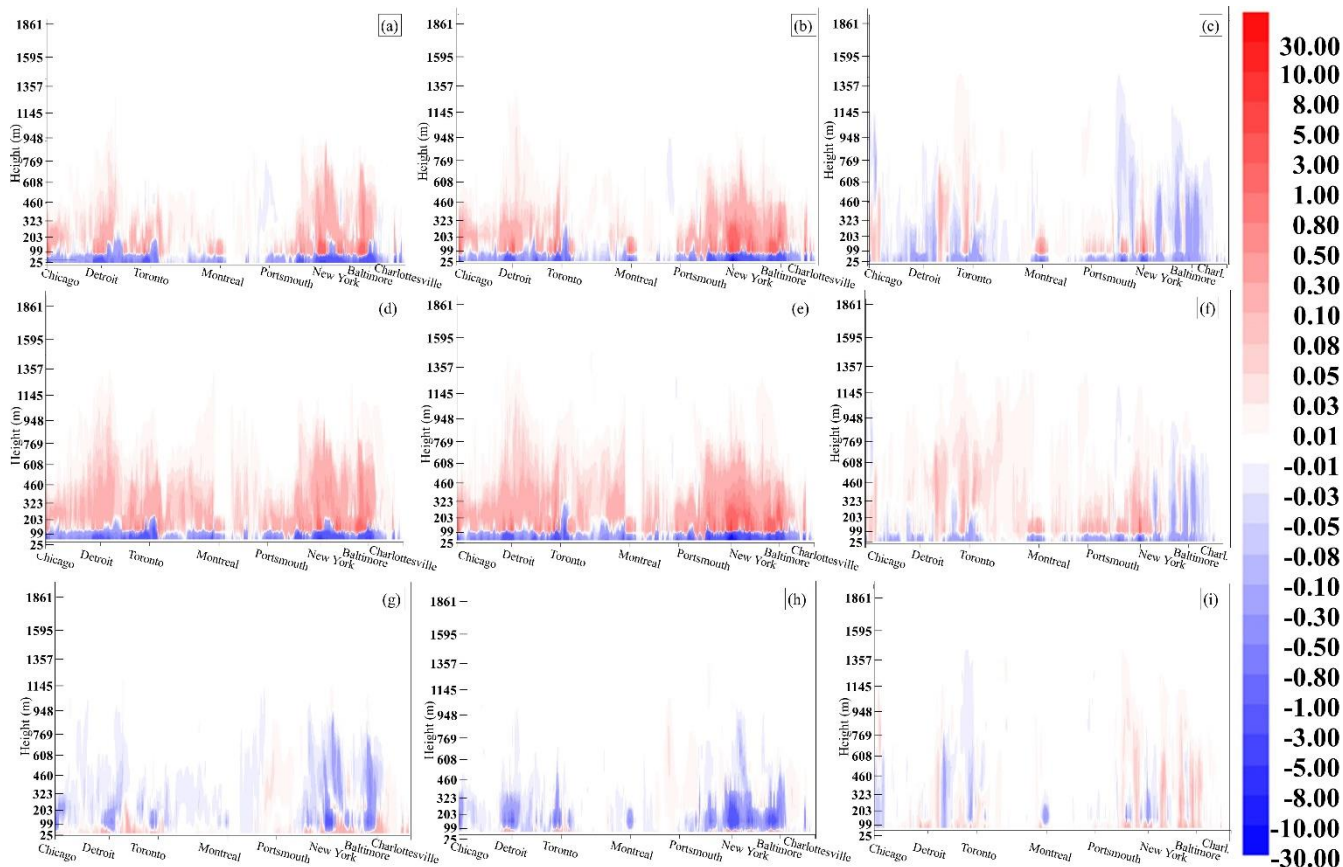
Figure 11. Vertical cross-sections of concentration differences between major eastern North American cities, January 2016, panels arranged as in Figure 10. Vertical coordinate: unitless hybrid, top-of-scale is approximately 2 km. Units: ΔNO$_2$, ΔO$_3$: ppbv. ΔPM2.5: μg m^{-3}.
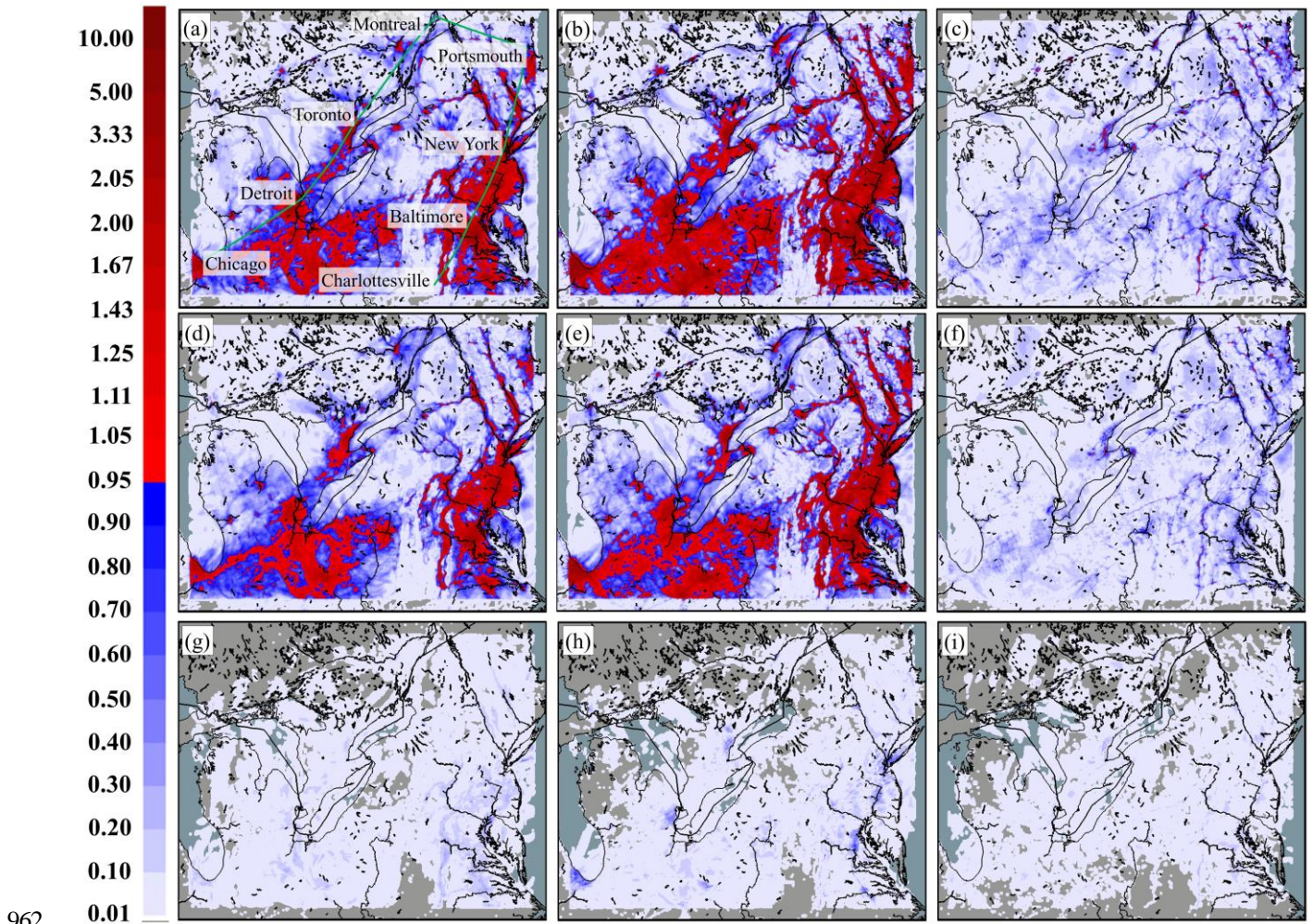
Figure 12. 90% confidence levels for the 30 day average surface NO_2, PM2.5 and O_3, January 2016, PanAm 2.5km grid cell size domain simulation. Panels arranged as in Figure 10: (10, 14, and 22UT) according to species; (a,b,c): NO_2; (d,e,f) PM2.5; (g,h,i) O_3 (ppbv). Green line in panel (a) indicates position of vertical cross-section shown in Figure 13. Values > 1.0 indicate that the simulations differ at greater than 90% confidence.
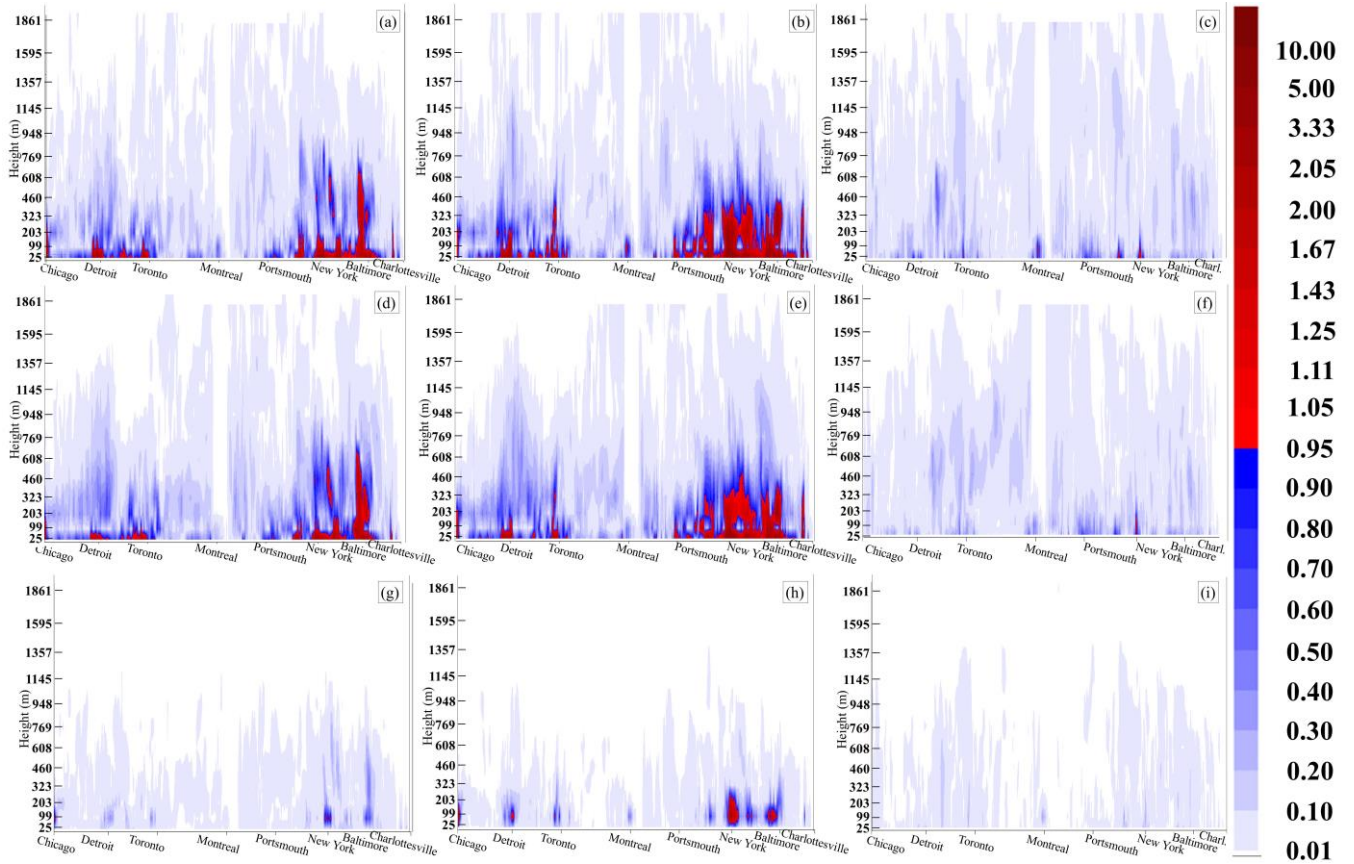
Figure 13. Vertical cross-sections of 90% confidence ratio values between major eastern North American cities, January 2016, panels arranged as in Figure 10. Values > 1.0 indicate that the simulations differ at greater than 90% confidence.

976
977 **Table 1.** Gaussian distribution fits of VIT TKE drop-off with height, from observation and CFD studies.

Study, Case	Slope	Intercept	R^2	Mixing length $(z \text{ at } e^{\left(-\frac{(z-h_q)^2}{2\sigma_q^2}\right)} = 0.01)$, m
Isolated vehicles:				
Rao *et al.* (2002), cube van, 50 mph, $h_q = 2$m	2.2452	1.8534	0.9856	3.53
Rao *et al.* (2002), cube van, 30 mph, h_q=2m	1.0230	1.4969	0.9709	4.22
Kim *et al.* (2016), lead automobile, $h_q = 1.5$m	4.6431	3.9013	0.8845	2.50
Kim *et al.* (2016), lead diesel cargo truck, h_q =4m	3.6143	4.2223	0.9355	5.13
Vehicle Ensembles:				
Kim *et al.* (2016), automobile immediately following lead diesel cargo truck, $h_q = 1.5$m	0.073529	4.1144	0.9801	9.41
Kim *et al* (2016), 2nd automobile, following lead diesel cargo truck, $h_q = 1.5$m	0.47337	3.9275	1.00[a]	4.60
Kim *et al.* (2016) 2nd diesel cargo truck, $h_q = 4$m	0.04070	4.7935	0.5424	14.64
Woodward *et al.* (2019) vehicle ensemble[b], h_q=1.5m, parallel to flow, right lane	0.01916	-1.2402	0.9135	17.01
Woodward *et al.* (2019) vehicle ensemble[b], $h_q = 1.5$m, parallel to flow, left lane	0.01155	-1.4532	0.7543	21.46
Woodward *et al.* (2019) vehicle ensemble[b], $h_q = 1.5$m, transverse to flow, right lane	0.012489	-1.4766	0.9667	20.70
Woodward *et al.* (2019) vehicle ensemble[b], $h_q = 1.5$m, transverse to flow, left lane	0.0098094	-1.7815	0.9536	23.16
Zhang *et al.* (2017), VS1: $h_q = 1.6$m, vehicle speed = 9 km hr^{-1}, Wind 11 km hr^{-1}	0.0029165	5.1706	0.6614	41.24
Zhang *et al.* (2017), VS2: $h_q = 1.6$m, speed = 36 km hr^{-1}, Wind 11 km hr^{-1}	0.005158	5.0964	0.8306	31.38
Zhang *et al.* (2017), VS3: $h_q = 1.6$m, vehicle speed = 36 km hr^{-1}, Wind 36 km hr^{-1}	0.007298	6.3394	0.9006	26.62
Zhang *et al.* (2017), VS4: $h_q = 1.6$m, vehicle speed = 36 km hr^{-1}, Wind 36 km hr^{-1}	0.005411	5.6387	0.9339	30.67
Zhang *et al.* (2017), VS5: $h_q = 1.6$m, vehicle speed = 36 km hr^{-1}, Wind 54 km hr^{-1}	0.003478	4.3150	0.8574	37.89

978
979 a. Note that only two contour lines were available for retrieving TKE and height values from this vehicle within Figure 14 of Kim
980   et al. (2016); while the correlation coefficient is formally unity, this is a two-point line.
981 b. Woodward et al. (2019) Figure 21 turbulent velocity components in the parallel and transverse directions were squared, and
982   distances were scaled to give equivalent distances from wind-tunnel to ambient environment.
983

984

Table 2. Model performance for NO_2, PM2.5, and O_3, 10km grid cell size North American domain. No VIT refers to simulation without vehicle-induced turbulence, VIT refers to the simulation incorporating vehicle-induced turbulence. **Bold-face** print identifies the better score, italics the worse score, and regular font indicates similar performance, between the two simulations, for each metric and chemical species compared.

Species	Evaluation Metric	North America		Canada		USA	
		No VIT	VIT	No VIT	VIT	No VIT	VIT
NO_2 (ppbv)	FAC2	*0.449*	**0.474**	*0.437*	**0.464**	*0.461*	**0.484**
	MB	*1.195*	**0.142**	*1.553*	**0.716**	*0.860*	**-0.396**
	MGE	*4.226*	**3.542**	*3.679*	**3.057**	*4.738*	**3.996**
	NMGE	*0.832*	**0.698**	*0.911*	**0.757**	*0.783*	**0.661**
	r	**0.515**	*0.511*	**0.520**	*0.518*	**0.507**	*0.506*
	RMSE	*7.089*	**5.665**	*6.058*	**4.764**	*7.934*	**6.396**
	COE	*-0.083*	**0.092**	*-0.238*	**-0.029**	*-0.017*	**0.142**
	IOA	*0.459*	**0.546**	*0.381*	**0.486**	*0.492*	**0.571**
PM2.5 ($\mu g\ m^{-3}$)	FAC2	*0.451*	**0.453**	*0.402*	**0.412**	**0.466**	*0.465*
	MB	**-2.116**	*-2.619*	**-0.032**	*-0.669*	**-2.688**	*-3.154*
	MGE	*4.982*	**4.733**	*4.733*	**4.237**	*5.043*	**4.864**
	NMGE	*0.672*	**0.638**	*0.879*	**0.787**	*0.632*	**0.610**
	r	*0.185*	**0.211**	*0.147*	**0.163**	*0.217*	**0.241**
	RMSE	*7.933*	**7.300**	*8.870*	**7.323**	*7.628*	**7.271**
	COE	*-0.203*	**-0.143**	*-0.431*	**-0.281**	*-0.188*	**-0.146**
	IOA	*0.399*	**0.429**	*0.285*	**0.360**	*0.406*	**0.427**
O_3 (ppbv)	FAC2	*0.819*	**0.823**	*0.760*	**0.767**	*0.830*	**0.833**
	MB	*-0.097*	**0.080**	*-3.652*	**-3.498**	**0.503**	*0.684*
	MGE	*10.050*	**10.009**	*8.111*	**8.023**	*10.379*	**10.346**
	NMGE	*0.325*	**0.323**	*0.343*	**0.339**	*0.322*	**0.321**
	r	0.707	0.707	*0.703*	**0.705**	0.694	0.694
	RMSE	*13.095*	**13.035**	*10.357*	**10.242**	*13.511*	**13.458**
	COE	*0.239*	**0.242**	*0.144*	**0.153**	*0.229*	**0.232**
	IOA	*0.619*	**0.621**	*0.572*	**0.577**	*0.615*	**0.616**

991 **Table 3.** Model performance for NO_2, PM2.5, and O_3, 2.5 km grid cell size Pan Am domain. No VIT refers to simulation without vehicle-
992 induced turbulence, VIT refers to the simulation incorporating vehicle-induced turbulence. **Bold-face** print identifies the better score, italics
993 the worse score, and regular font indicates similar performance, between the two simulations, for each metric and chemical species compared.

Species	Evaluation Metric	PanAm Domain July		PanAm Domain January	
		No VIT	VIT	No VIT	VIT
NO_2 (ppbv)	FAC2	*0.584*	**0.593**	**0.714**	*0.711*
	MB	*1.005*	**0.386**	*0.852*	**-0.328**
	MGE	*4.137*	**3.866**	*5.166*	**5.146**
	NMGE	*0.670*	**0.626**	*0.457*	**0.455**
	r	**0.560**	*0.543*	**0.736**	*0.693*
	RMSE	*6.909*	**6.373**	*7.917*	**7.892**
	COE	*0.059*	**0.121**	*0.348*	**0.350**
	IOA	*0.530*	**0.560**	*0.674*	**0.675**
PM2.5 ($\mu g\ m^{-3}$)	FAC2	**0.573**	*0.569*	*0.563*	**0.592**
	MB	**-2.669**	*-3.055*	*3.930*	**2.362**
	MGE	*5.813*	**5.729**	*8.315*	**7.012**
	NMGE	*0.537*	**0.529**	*0.865*	**0.729**
	r	*0.338*	**0.346**	*0.163*	**0.170**
	RMSE	*8.972*	**8.791**	*24.875*	**23.194**
	COE	*-0.077*	**-0.061**	*-0.463*	**-0.234**
	IOA	*0.462*	**0.467**	*0.269*	**0.383**
O_3 (ppbv)	FAC2	*0.831*	**0.832**	*0.852*	**0.854**
	MB	**4.138**	*4.213*	**1.652**	*1.731*
	MGE	**10.640**	*10.648*	*6.433*	**6.427**
	NMGE	0.333	0.333	0.259	0.259
	r	0.709	0.709	**0.688**	*0.687*
	RMSE	**13.826**	*13.838*	*8.440*	**8.427**
	COE	0.146	0.146	*0.190*	**0.191**
	IOA	0.573	0.573	*0.595*	**0.596**

994
995